Wind tunnel measurements of the aerodynamic characteristics of a 3:2 rectangular cylinder including non-Gaussian and non-stationary features

Cung H. Nguyen[1], Dinh T. Nguyen[2], John S. Owen *[1] and David M. Hargreaves[1]

[1]Faculty of Engineering, University of Nottingham, Nottingham, NG7 2RD, UK

[2]RWDI UK, Milton Keynes MK11 3LH, UK

*Corresponding author: John.Owen@nottingham.ac.uk

This preprint has been accepted for Journal of Wind Engineering and Industrial Aerodynamics

Abstract

This paper presents a wind tunnel investigation of the aerodynamic characteristics (force and pressure coefficients) of a static 3:2 rectangular cylinder in smooth flow for angles of attack between -4° and 90° at various values of Reynolds number. In contrast to much of the existing literature, this study shows clear dependence of the mean drag coefficients on Reynolds number. In addition, the variation of aerodynamic parameters with angle of attack is fully mapped for a symmetric section revealing that the peak values of the mean values of drag, lift, moment and Strouhal number do not occur at the same critical angle of attack.

The present study also presents the first map for identifying the locations of the reattachment and stagnation points as well as the zones of angle of attack where the flow is separated and attached on a face of the section. The phenomenon of switching flow is observed at the angle of attack 25°, leading to strong non-stationarity and non-Gaussian distributions of the aerodynamic forces and pressure. Another phenomenon, so-called unsteady low-frequency vortex shedding, is also observed at higher angles of attack. These phenomena need to be accounted for when estimating wind loading and aeroelastic instability for these sections.

Keyword: 3:2 rectangular section, wind tunnel, non-Gaussian, non-stationary, bimodal distribution, Strouhal number, galloping, VIV, low-frequency vortex

1 Introduction

Many structural elements and civil structures have rectangular sections. These bluff bodies are prone to aerodynamic instability phenomena such as vortex-induced vibration (VIV) and galloping, depending on their side ratios $B : D$ (B and D are the along wind width and cross wind depth of the cross section, respectively). In the literature, a number of studies have investigated the aerodynamic forces on and pressure distribution around rectangular cylinders as well as the characteristics of the flow field around the bodies. These studies have typically been conducted by means of wind tunnel tests and Computational Fluid Dynamics (CFD) simulations for different side ratios and angles of attack, denoted as α.

Most of these studies have focused on square section cylinders with sharp corners, starting with the wind tunnel experiments by Vickery (1966) who measured aerodynamic pressures and Strouhal number (St) for a range of angles of attack. Later studies have investigated the features of drag and lift forces, pressure distributions, vortex shedding and flow patterns (Lee, 1975; Rockwell, 1977; Okajima, 1982; Obasaju, 1983; Igarashi, 1984; Knisely, 1990; Norberg, 1993; Saha et al., 2000; Dutta et al., 2003; Luo et al., 2007; Huang et al., 2010; Carassale et al., 2014; Nguyen et al., 2020a). One of the important findings from these studies is the existence of the so-called critical angle of attack, denoted as α_{cr} (some studies used the terminology reattachment angle of attack), from which two flow regimes are clearly distinguished, resulting in sudden changes in the mean drag and lift coefficients and the Strouhal number. The flow is separated from both the top and bottom faces for $\alpha < \alpha_{cr}$, whereas it reattaches on the bottom face, i.e. the face exposed to the wind (it is considered that α positive is in the clockwise direction for flow from the left), for $\alpha \geq \alpha_{cr}$, leaving a smaller separation bubble near the leading edge (Figure 1). The drag and lift coefficients have negative slopes for $\alpha < \alpha_{cr}$, reach the minimum values at $\alpha = \alpha_{cr}$ and have positive slopes for $\alpha > \alpha_{cr}$. Also, the Strouhal number increases as α increases to α_{cr}, reaching a maximum value at $\alpha = \alpha_{cr}$ and remaining almost constant for $\alpha > \alpha_{cr}$.

Also, for the studies on square cylinders, Carassale et al. (2014) first observed that there is an intermittent behaviour at α_{cr}, where the flow switches between two flow regimes. This behaviour was examined through the time history of the lift force, showing two dominant frequencies changing in time. The behaviour was seen for a certain section with rounded corners, depending on Reynolds number (Re), and was not visible for a square section with sharp corners. The behaviour was explained as a result of the intermittent reattachment of the flow on the bottom face at the critical angle of attack α_{cr}.

For cylinders with other side ratios, most of the studies have focused on the case of zero angle of attack (e.g. Okajima, 1982; Matsumoto, 1996; Bruno et al., 2014; Ito et al., 2015; Nguyen et al., 2018; Álvarez et al., 2019). Norberg (1993) conducted wind tunnel experiments on rectangular

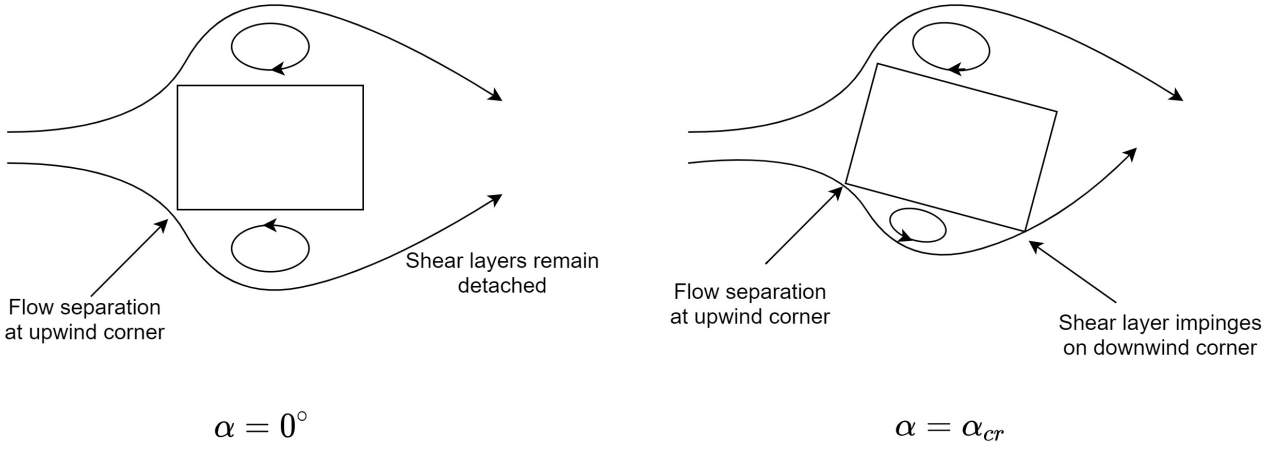

Figure 1: Schematic representation of shear layer separation and impingement at critical angle of attack

sections for side ratios $B : D = 1$, 1.62, 2.5 and 3 and for a large range of angles of attack to investigated the behaviour of aerodynamic forces and pressure as well as flow field. The study showed qualitative similarity to the case of sharp square section cylinders in terms of the variation of drag and lift coefficients, Strouhal number and flow field with the angle of attack.

There is little information on the characteristics of aerodynamic force and pressure, vortex shedding and flow field of rectangular section cylinders with a side ratio of 3:2, although there is relatively rich information on those for other side ratios. This cylinder represents many existing tall buildings and was selected as one of the benchmark tall buildings by the Commonwealth Advisory Aeronautical Council (CAARC) (Holmes and Tse, 2014). For this particular section, Mannini et al. (2014) used wind tunnel tests to estimate drag and lift coefficients for Re = 143 000 and Strouhal number, estimated from the lift force, for Re = 24 000 to 143 000, all for a range of angles of attack between -16° and 16°. The study showed that there is no dependence of drag and lift forces and Strouhal number on Reynolds number, except for the root-mean-square (RMS) of the fluctuation of the lift force. Moreover, α_{cr} is about 9°. Also considering the 3:2 rectangular section, Massai et al. (2018) reported Strouhal number for Re = 1058 to 9299 through water tank experiments, stating that Strouhal number shows a small dependency on Reynolds number and α_{cr} is about 7.5°. It is worth noting from these two studies that neither measurements of pressure distribution nor analysis of flow features were presented. The change of the pattern of force coefficients and Strouhal number around the critical angle of attack were explained through reference to the observations in Norberg (1993) and to other cases of square section cylinders.

The motivation of the current study starts from the aim of developing a novel and holistic risk-based framework to improve the resilience of infrastructure in typhoons. Such a framework combines key components of (i) a probabilistic model of the typhoon hazard (Nguyen et al., 2020b); (ii) aeroelastic models (e.g. vortex-induced vibrations, galloping) of slender columns in

power line networks; (iii) vulnerability and cost models of slender structures failed in typhoons. The current paper addresses (ii) in particular, where a better understanding of the dynamic and aerodynamic behaviour of slender vertical structures in winds from a full range of wind directions is required. Given the limited data available, this paper presents further insights into the aerodynamics of a 3:2 rectangular section. This is considered typical of many poles use in power distribution, lighting and communications networks where rectangular sections in the range 1:1 to 2:1 are frequently used in Vietnam, based on the first author's experience. The insights are achieved through a series of wind tunnel tests on a 3:2 rectangular cylinder to measure the aerodynamic forces and surface pressure in smooth flow and for a wide range of angles of attack. The aerodynamic coefficients obtained can be used for modelling the wind-excited response (e.g. buffeting) and aeroelastic instability (e.g. galloping) of slender structures (e.g. poles and towers) in analysing the risks from typhoons.

The paper is structured as follows: Section 2 describes the testing setup; Sections 3, 4, and 5 present the aerodynamic forces (drag, lift and moment) coefficients, Strouhal number and the aerodynamic pressure coefficients obtained from the tests, respectively; Section 6 identifies flow features based on the aerodynamic force and pressure characteristics; Section 7 presents further analysis of non-stationary and non-Gaussian flow and the switching flow phenomenon; the impact of these features on engineering applications will be discussed in Section 8; and, finally, Section 9 draws critical remarks from the study.

2 Wind Tunnel Test Setup

Wind tunnel tests on a section model of a 3:2 rectangular cylinder were carried out in the Atmospheric Boundary Layer (ABL) wind tunnel of the University of Nottingham (Figure 2a). This wind tunnel has a blow down configuration with an enclosed working section and an open return. The tunnel has a length of 14.5 m between the end of the contraction and the start of the diffuser, resulting in a fetch of 12.5 m to the mid-line of the 2 m turntable. The working section is 2.4 m wide by 1.8 m high. Although the wind tunnel was designed as an ABL facility for building aerodynamic studies, when the turbulence generators are removed the turbulence intensity of the flow at the end of the contraction has been measured to be less than 0.2%. Hence, it is possible to configure the tunnel for aerodynamic tests on section models in smooth wind flow with an operating velocity range of $U = 1\,\mathrm{m\,s^{-1}}$ to $11.5\,\mathrm{m\,s^{-1}}$.

The sectional model of the 3:2 rectangular cylinder was manufactured from plywood due to the ease of manufacture and closer dimensional control. The section was designed to be light and rigid, with two aluminium spines and internal diaphragms providing sufficient stiffness to ensure that vortex shedding did not lead to any local or flexural vibrations. The surface of the cylinder was prepared carefully to ensure a smooth finish with an estimated roughness (arithmetic mean

deviation of profile) $R_a \leq 10\,\mu$m. The cylinder had dimensions: length $L = 1.6\,$m, width of cross section $B = 0.15\,$m and depth of cross section $D = 0.1\,$m. Therefore, the aspect ratio varied from 16 ($\alpha = 0°$) to 10.7 ($\alpha = 90°$), both of which are within the range of values presented in the literature for wind tunnel tests on rectangular sections (Yang and Mason, 2019; Mannini et al., 2014; Norberg, 1993). Rectangular end plates were provided measuring 450 mm by 300 mm, after (Mannini et al., 2018), which were made from thin aluminium plate. The model was instrumented with 64 pressure taps arranged in an array of four rings (Figure 2b). Each ring has 16 taps distributed around the cross section as shown in Figure 2c. The pressure taps were connected to a Scannivalve MPS4264 miniature pressure scanner to collect pressure measurements at a sampling rate of 500 Hz.

For the static tests, the model was rigidly supported in the horizontal position on a force measurement system installed within the aerodynamic working section of the wind tunnel. The angle of attack of the section was measured using a digital level and adjusted by rotating the model about a central pivot. The force measurement system was assembled at the University of Nottingham and comprised 6 single axis load cells OBUG from Applied Measurements Limited. A sampling rate of 500 Hz was used to collect the force measurements.

The model was tested in smooth flow to enable comparisons with other tests in the literature (Mannini et al., 2018; Massai et al., 2018; Norberg, 1993) at four different Reynolds numbers (normalised by the cross wind depth D): Re = 25 000 (3.8 ms^{-1}), 38 000 (5.7 ms^{-1}), 51 000 (7.7 ms^{-1}) and 63 000 (9.5 ms^{-1}). The angle of attack α (Figure 2d) was varied from -4° to 90°, which fully mapped the behaviour of the section if it were assumed to be symmetrical. Fine increments of α were used between -4° and 20° and around 70° to capture the critical angles of attack. Larger increments were used from 20° to 70° and close to 90°. At each wind speed and angle of attack, 60-second time histories of aerodynamic forces and surface pressures were recorded. This process was repeated five times to evaluate the standard error and confidence limits of measured quantities; the error bars in subsequent plots represent 99.7% confidence levels of the mean value.

The results from the current tests are mainly compared with those from Mannini et al. (2018), in which wind tunnel tests were conducted on a rectangular section prism with the same aspect ratio, but at a higher Reynolds number.

3 Aerodynamic Force Coefficients

The aerodynamic force coefficients for drag $C_D(t)$, lift $C_L(t)$ and moment $C_M(t)$ are determined from the force balance measurements and are defined as

$$C_D(t) = \frac{2F_D(t)}{\rho D L \bar{U}^2}; \quad C_L(t) = \frac{2F_L(t)}{\rho D L \bar{U}^2}; \quad C_M(t) = \frac{2M(t)}{\rho D^2 L \bar{U}^2} \tag{1}$$

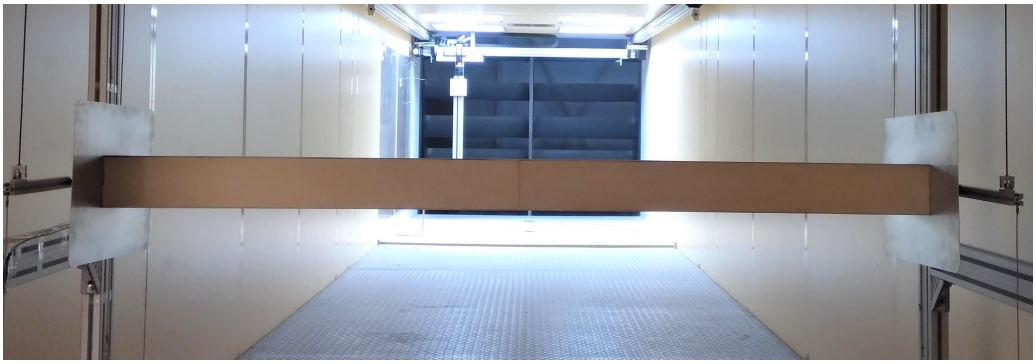

(a)

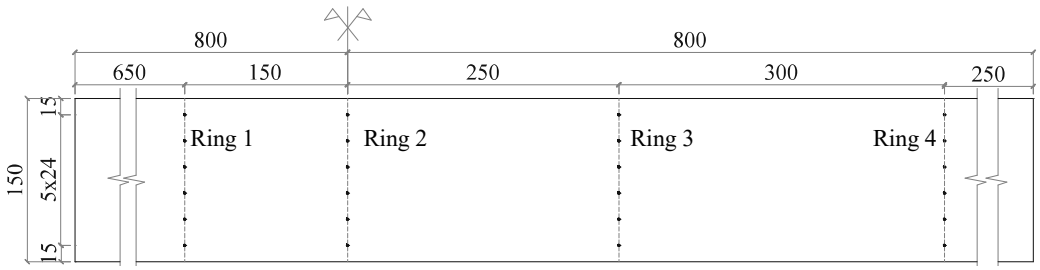

(b)

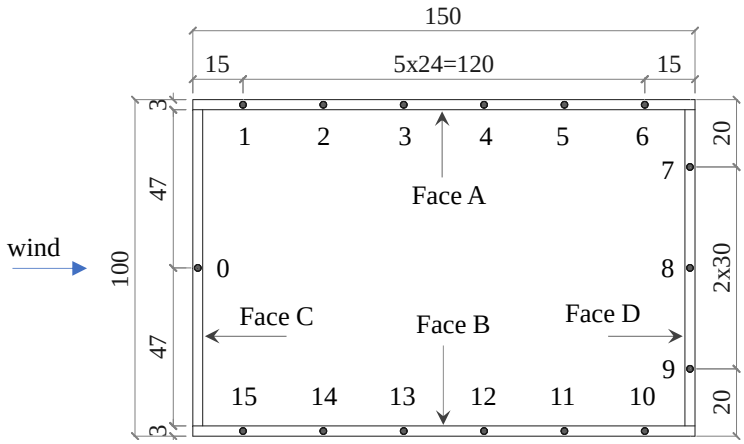

(c)

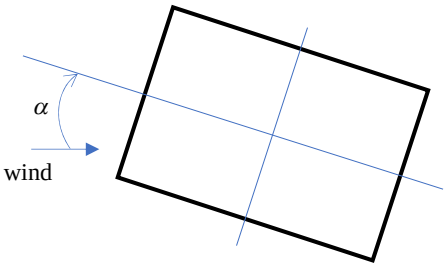

(d)

Figure 2: Test setup: (a) the sectional model in the wind tunnel; (b) location of pressure rings along the cylinder axis; (c) arrangement of pressure taps in a ring; (d) definition of angle of attack α. (Units for linear dimensions: mm)

where $\rho, \bar{U}, F_D, F_L$ and M are the air density, mean wind speed, drag force, lift force and moment, respectively.

3.1 Drag Coefficient

Figure 3a shows the variation of mean values of the drag coefficients, $\bar{C}_D$, with angles of attack α in the range from $-4°$ to $90°$. For Re = 51 000 and 63 000 and the particular case of $\alpha = 25°$, there is a jump in time history of C_D as shown in Figure 4. Therefore, it is misleading to evaluate the mean value of $C_D(t)$ for the whole time record. Instead, a mean value is evaluated for each of the upper and lower branches of $C_D(t)$. The upper and lower $\bar{C}_D$ for different Reynolds numbers are re-plotted in Figure 3 with the square and diamond markers, respectively. The upper and lower means are plotted at $\alpha = 26.5°$ instead of $\alpha = 25°$ to improve clarity by avoiding the circle, square and diamond markers overlapping at $\alpha = 25°$. The physical meaning of the jump phenomenon is to be discussed later in Section 7.2.

It can be seen from Figure 3a that the mean drag coefficients are dependent on Reynolds number for all tested angles of attack. The dependence is shown in Figure 5 for selected angles of attack, where in each case the coefficients decrease for increasing Reynolds number. In the case of circular sections or sections with rounded corners, such Reynolds number dependency is related to movement of the separation points. It can therefore be influenced by factors including surface roughness (e.g. Carassale et al., 2014; Demartino, C. and Ricciardelli, F., 2017) and turbulence. However, since the separation points in the current study are determined by the sharp corners of the section, the reasons for this Reynolds number dependency are not immediately apparent. It is likely that they are related to the width of the wake and its effect on the pressures on the downwind faces of the cylinder. However, further work is required to confirm this and to determine whether turbulence and surface roughness have an influence on the Reynolds dependence by affecting flow reattachment and flow within regions of re-circulation.

The variation of $\bar{C}_D$ with respect to α can be classified into four regions. $\bar{C}_D$ decreases as α increases from $0°$ to $8.3°$, at which $\bar{C}_D$ is a minimum. Between $\alpha = 8.3°$ and $\alpha = 25°$, $\bar{C}_D$ rises sharply. Between $\alpha = 25°$ and $\alpha = 70°$, the value of $\bar{C}_D$ changes only slightly from the lower mean $\bar{C}_D$ at $\alpha = 25°$. There is another α_{cr} at $\alpha = 70°$, from where $\bar{C}_D$ reduces towards $\alpha = 90°$, which is the zero angle of attack for the 2:3 configuration.

In a comparison with the results reported by Mannini et al. (2018), the present study shows comparable $\bar{C}_D$ for the angles of attack in the range from $\alpha = -4°$ to $\alpha = 16°$, with the difference in magnitude consistent with the Reynolds number dependence. Outside this range, the data is not available in the study by Mannini et al. (2018). The current study agrees very well (within $0.7°$) with value of $9°$ for the critical angle of attack given in Mannini et al. (2018), and this

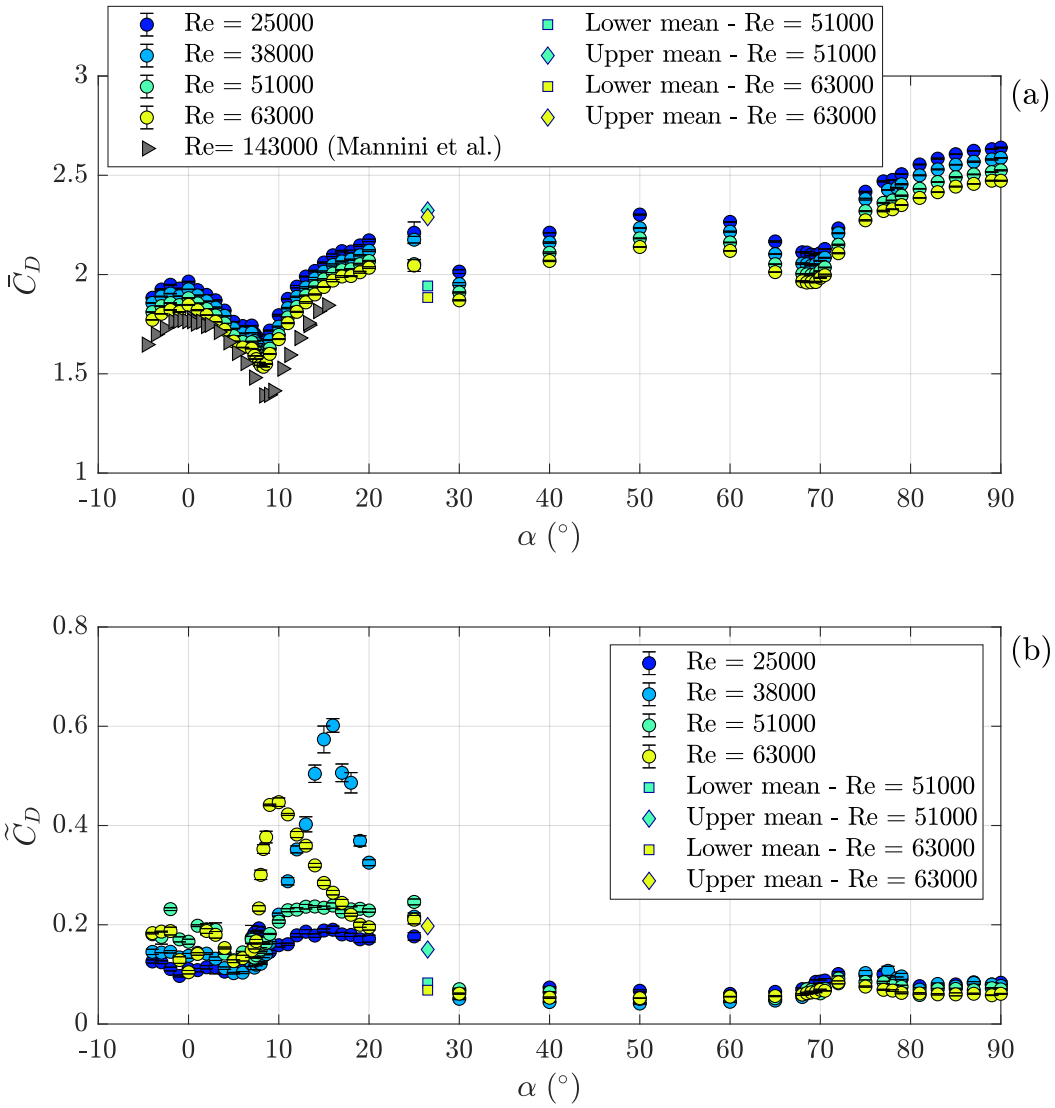

Figure 3: Variation of (a) mean drag coefficient, $\bar{C}_D$, and (b) RMS drag coefficient, $\widetilde{C}_D$ with respect to α. (Note, upper and lower values of mean at 25° are plotted at 26.5° for clarity).

.

difference can be explained by the difference in Reynolds number and also the uncertainty in measuring the angle of attack.

Figure 3b shows the root-mean-square (RMS) of the fluctuations of the drag coefficients, $\widetilde{C}_D$. Similar to the mean drag coefficients, $\widetilde{C}_D$ is dependent on Reynolds number. The results from the wind tunnel tests show that $\widetilde{C}_D$ and its dependence on Reynolds number are small for the angles of attack equal to and higher than 30°, but noticeable for lower angles of attack. For most of the tested Reynolds numbers, $\widetilde{C}_D$ sharply increases to and decreases from a maximum peak value at a specific angle of attack. It is $\alpha = 7.8°$, $\alpha = 16°$, and $\alpha = 10°$ for Re = 25 000, Re = 38 000, and Re = 63 000 respectively. A peak is unclear for the case of Re = 51 000. There is a sharp reduction in $\widetilde{C}_D$ after $\alpha = 25°$ and the fluctuations remain small up to $\alpha = 65°$. Fluctuations rise slightly from $\alpha = 70°$ to a low peak at $\alpha = 75°$.

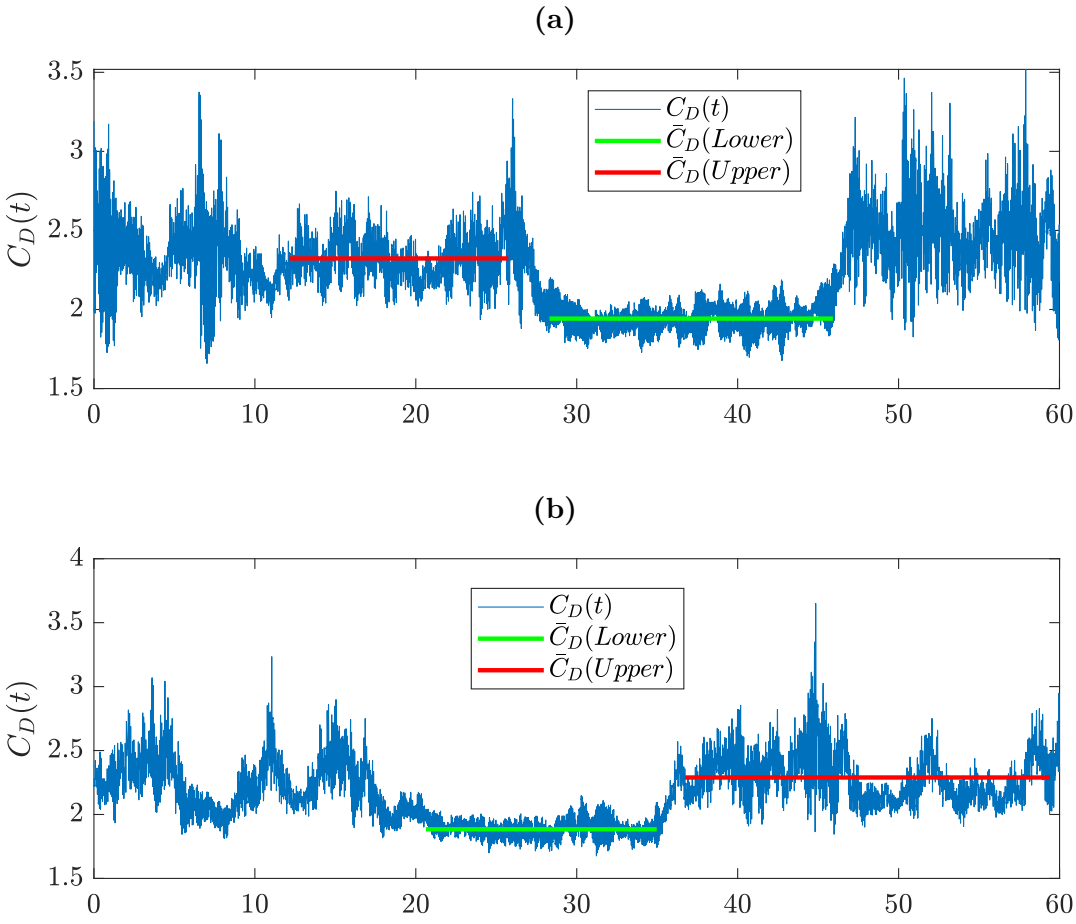

Figure 4: Time history of $C_D(t)$ for $\alpha = 25°$ for (a) Re=51 000 and (b) Re=63 000

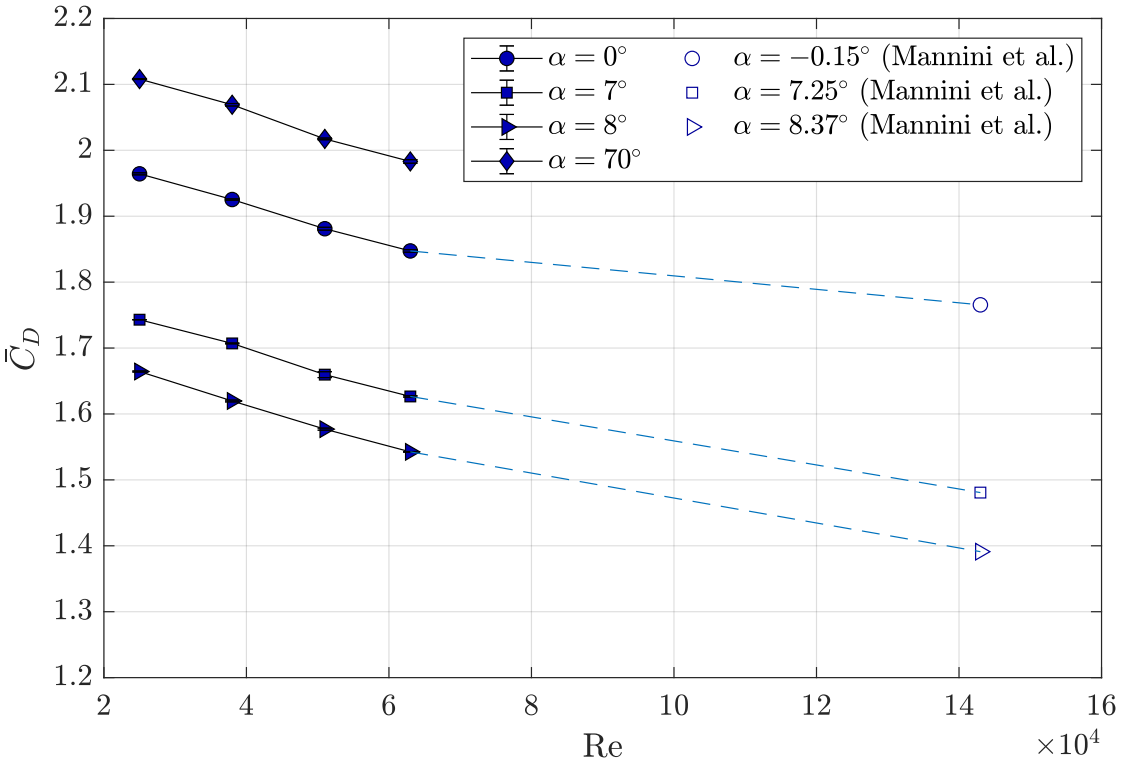

Figure 5: Variation of the mean drag coefficient, $\bar{C}_D$ with respect to Reynolds number (note that values of α from (Mannini et al., 2018) differ slightly from those in the current work)

3.2 Lift Coefficient

Figure 6a and Figure 6b show the mean lift coefficients, $\bar{C}_L$, and the RMS of the lift coefficients, $\widetilde{C}_L$, respectively. In contrast to the drag coefficients, no clear dependence of $\bar{C}_L$ on Reynolds number is observed, and there is only a slight dependence of $\widetilde{C}_L$ on Reynolds number. For angles of attack from $-4°$ to $19°$, there is agreement between the results of $\bar{C}_L$ obtained from the present wind tunnel tests and Mannini et al. (2018).

The mean lift coefficient displays abrupt changes at the same critical angles of attack as the case of $\bar{C}_D$, the minimum peak $\bar{C}_L$ is at $\alpha = 8.3°$ and the maximum at $\alpha = 70°$. Considering $\widetilde{C}_L$, the pattern is similar for different values of Reynolds number, although the magnitudes are different. There is a strong peak at $\alpha = 0°$ and a minimum at $\alpha = 7°$. There is a sharp drop in $\widetilde{C}_L$ after $\alpha = 25°$ and the fluctuations remain small up to $\alpha = 90°$.

3.3 Moment Coefficient

Figure 7a shows the mean moment coefficients, $\bar{C}_M$. Similar to $\bar{C}_L$, $\bar{C}_M$ is not dependent on Reynolds number. However, in contrast to the cases of $\bar{C}_D$ and $\bar{C}_L$, the minimum and maximum peaks of $\bar{C}_M$ occur at $\alpha = 11°$ and $\alpha = 65°$, respectively. These peaks are also less sharp than those in $\bar{C}_D$ and $\bar{C}_L$ and there is no plateau region evident between $\alpha = 25°$ and $\alpha = 65°$.

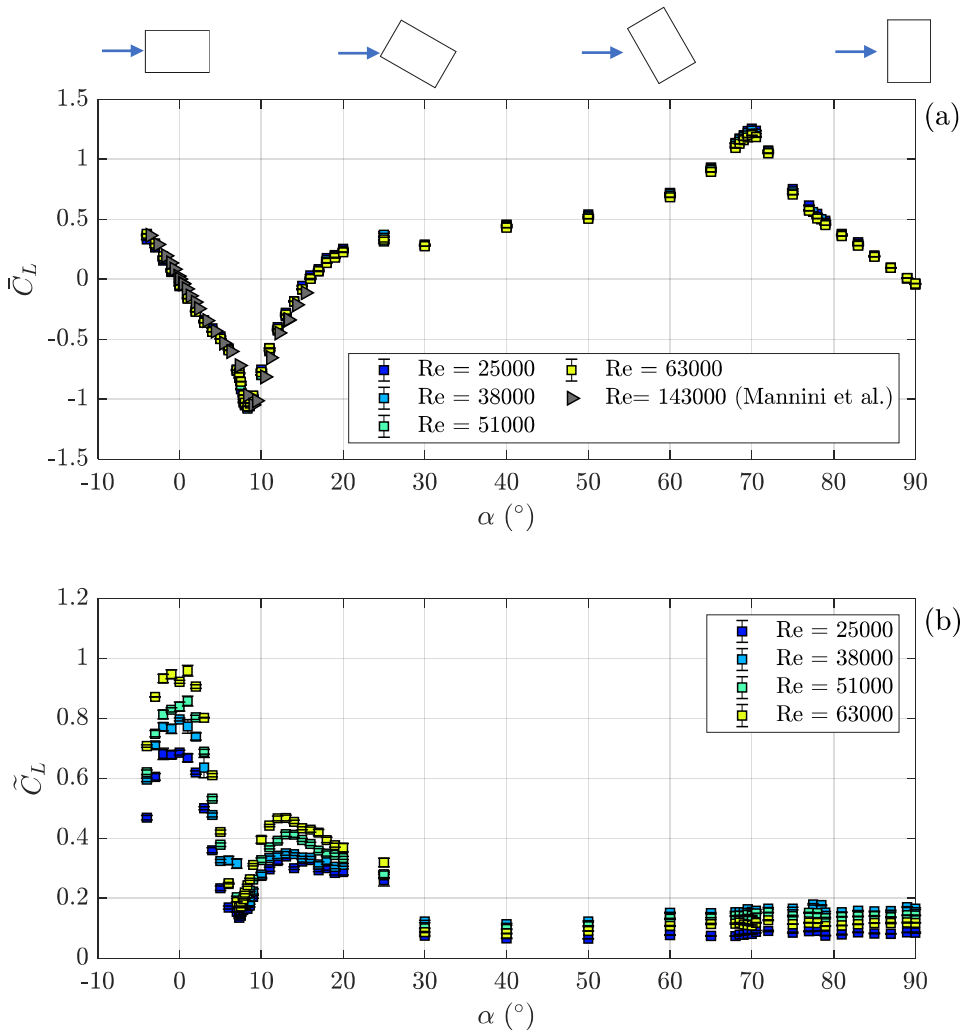

Figure 6: Variation of (a) mean lift coefficient, $\bar{C}_L$, and (b) RMS lift coefficient, $\widetilde{C}_L$ with respect to α

.

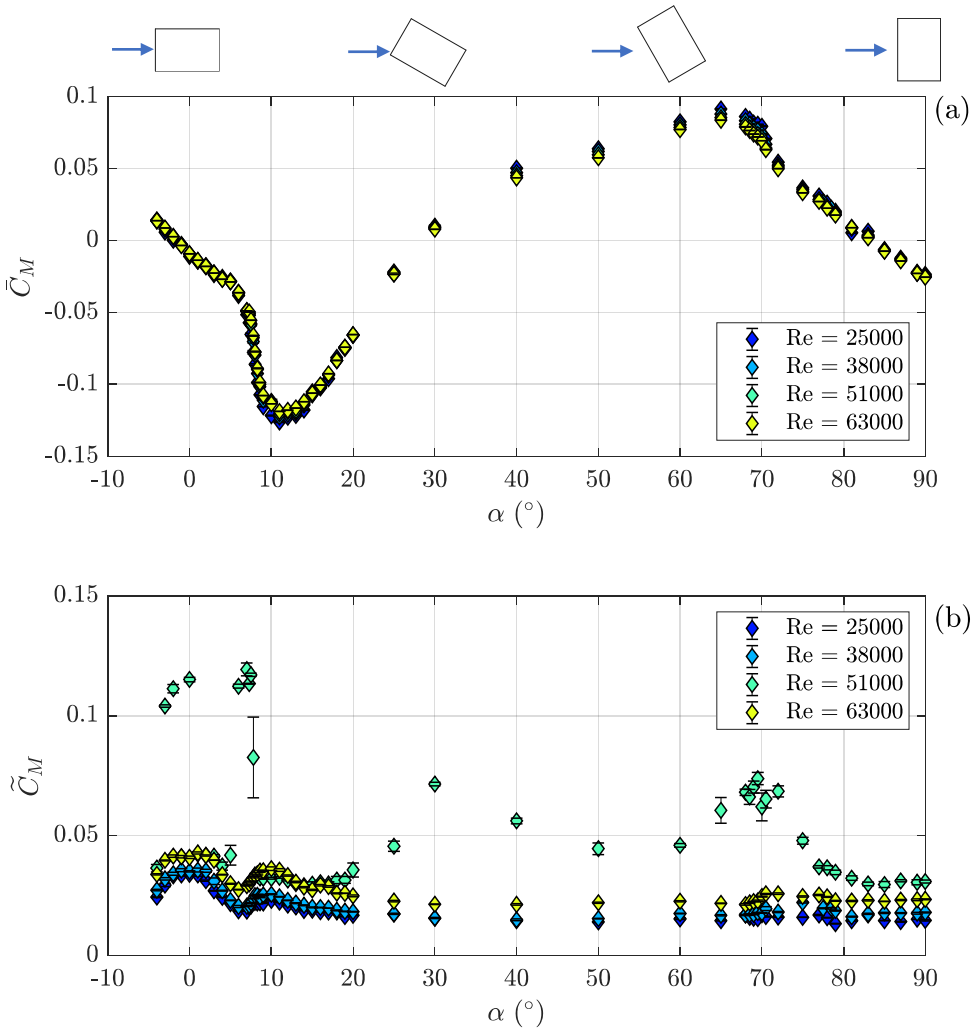

Figure 7: Variation of (a) mean moment coefficient, $\bar{C}_M$, and (b) RMS moment coefficient, $\widetilde{C}_M$, with respect to α.

.

Instead, there is a continual increase in $\bar{C}_M$ up to the peak at $\alpha = 65°$.

Figure 7b shows the RMS of the moment coefficients, $\widetilde{C}_M$. $\widetilde{C}_M$ is dependent on Reynolds number, although the pattern is similar in each case. The exception is Re = 51 000, which shows larger fluctuations than the other cases for most angles of attack and a peak at $\alpha = 70°$. Furthermore, the value of $\widetilde{C}_M$ at $\alpha = 7.8°$ is indistinct. This is because $C_M(t)$ is non-stationary at Re = 51 000 and $\alpha = 7.8°$, while it is stationary for the other cases. The non-stationarity is illustrated in Figure 8, which shows two time histories of $C_M(t)$.

Finally, it can be seen that the absolute values of the moment coefficients $\bar{C}_M$ and $\widetilde{C}_M$ are smaller than 0.15, with $\widetilde{C}_M$ even smaller than 0.05 for Re = 25 000, 38 000 and 63 000. They are also significantly smaller than the drag and lift coefficients.

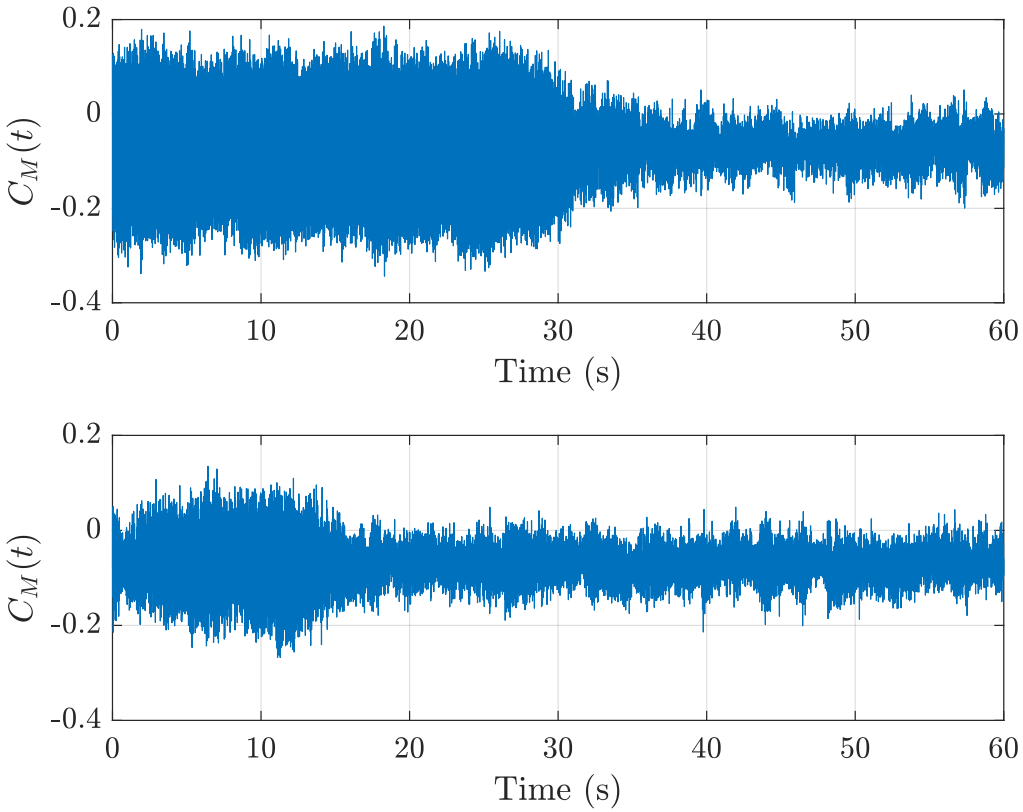

Figure 8: Example of two non-stationary time histories of $C_M(t)$ for Re=51 000 and $\alpha = 7.8°$

.

4 Strouhal Number

Figure 9 shows the variation of Strouhal number with respect to angle of attack and Reynolds number. The Strouhal number is defined as $\mathrm{St} = fD'/U$, where D' is the effective depth $D' = B\sin(|\alpha|) + D\cos(\alpha)$, and f is the frequency of vortex shedding, which is determined from the peak frequency of the power spectral density (PSD) of the lift force. These values of Strouhal number are compared with those estimated from the PSD of pressure at all the taps in Ring 1 to confirm that the estimation of Strouhal number is accurate. The results are compared with data from other wind tunnel experimental studies for rectangular cylinders, including Mannini et al. (2018) for a $B : D = 3 : 2$ section and Norberg (1993) for a $B : D = 1.62$ section, and from a water tank experiment for a $B : D = 3 : 2$ section by Massai et al. (2018).

It can be seen from the results of the present study that Strouhal number has a minimum value of 0.11 at $\alpha = 0°$ and increases steadily to a value of 0.135 at $\alpha = 9°$. At $\alpha = 9°$ there is a jump in value of Strouhal number to 0.19 and this value of Strouhal number is maintained for higher angles of attack up to $\alpha = 70°$. Above $\alpha = 70°$, Strouhal number starts decreasing. The abrupt change in Strouhal number at $\alpha = 9°$ is consistent with the critical angle of attack in the variation of $\bar{C}_D$ and $\bar{C}_L$ with α. Strouhal number also displays a slight dependence on Reynolds number for $\alpha \leq 25°$, where the Strouhal number is higher for lower Reynolds numbers. The

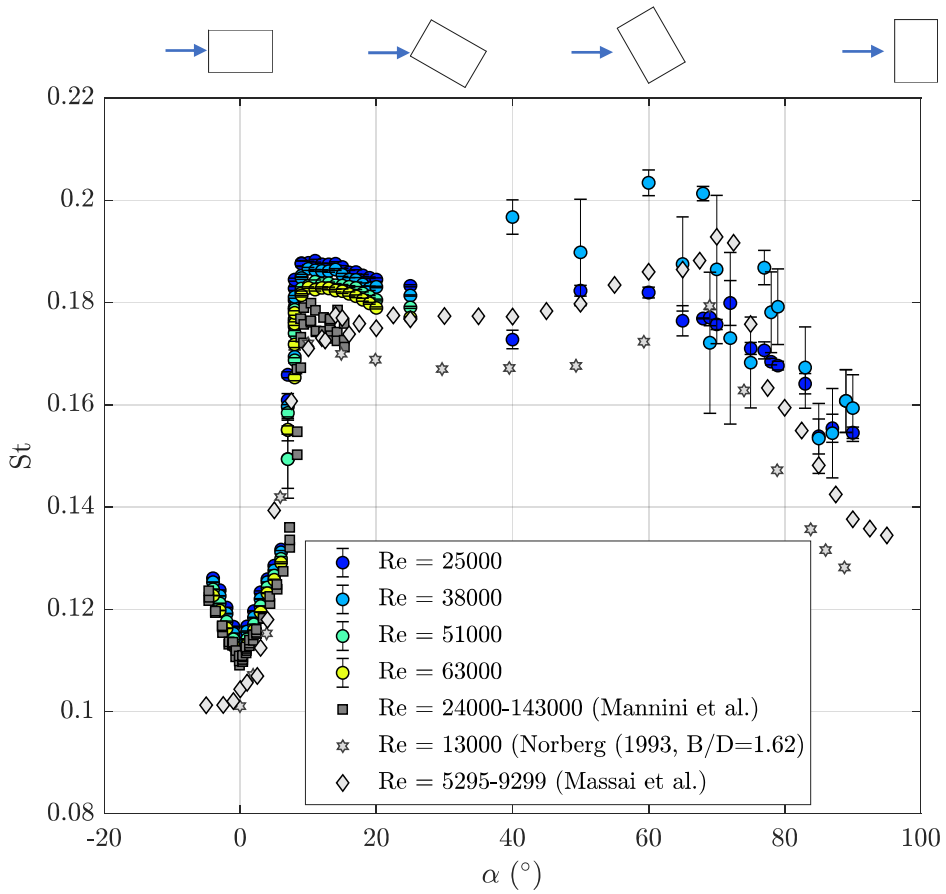

Figure 9: Variation of the Strouhal number with respect to the angle of attack and Reynolds number.

Reynolds dependency is apparent for $\alpha > 25°$, however Strouhal number is then lower for lower Reynolds number for most of the angles of attack.

Comparing the Strouhal number obtained from the present study with those from the other studies, the change of Strouhal number with respect to α has a similar trend for all the studies. A more detailed examination shows that the results of the present study are close to those obtained from the studies by Mannini et al. (2018); Massai et al. (2018) and Norberg (1993) for $0° < \alpha \leq 10°$. Outside of this range of angles of attack, there are clear differences in the measured values of Strouhal number. Here, it should be noted for the current study, only values of Strouhal number obtained for Re = 25 000 and 38 000 are shown in Figure 9 for $\alpha > 25°$. This is because there is no clear peak in the PSD of lift force or pressure for Reynolds number higher than 38 000 for $\alpha > 25°$. Furthermore, large uncertainty is evident in the estimates of Strouhal number for Re = 38 000. In contrast, the PSD of the lift force for $\alpha \leq 25°$ contains a clear peak for all values of Reynolds number considered and so estimates of Strouhal number contain very low uncertainty. These points are discussed further in Section 6.

5 Aerodynamic Pressure Coefficients

The aerodynamic pressure coefficient $C_p(t)$ is defined as follows

$$C_p(t) = \frac{2[p(t) - p_0]}{\rho \bar{U}^2} \tag{2}$$

where p and p_0 are the pressure measured at the pressure taps and static pressure respectively. The static pressure was measured using a pitot-static tube measuring the free stream upwind of the model.

Figure 10 shows the mean pressure coefficients, $\bar{C}_p$, at the 16 pressure taps around sensor ring 1 (see Figure 2) for different angles of attack and Reynolds number. In particular, Figure 10a shows $\bar{C}_p$ of taps 1 to 6, which are located on Face A of the section. Figure 10b shows $\bar{C}_p$ of taps 10 to 15 on Face B and Figure 10c shows $\bar{C}_p$ of tap 0 (Face C) and taps 7 to 9 (Face D). Generally, the variation of $\bar{C}_p$ with respect to angles of attack has similar features for all pressure taps on each face. Therefore, it is reasonable to investigate aerodynamic characteristics of the pressure on the section by looking at the characteristics of the pressure at one tap in ring 1 in each face. In the following, the investigation focuses on tap 6.

Figure 11 shows the variation of the mean pressure coefficients $\bar{C}_p$ with respect to angle of attack and Reynolds number at tap 6. The coefficients are dependent on Reynolds number and strongly variable for α from -4° to 20°, reaching a peak value at $\alpha = 7.3^\circ$. For α from 30° to 90°, the coefficients are also dependent on Reynolds number but less variable with respect to angle of attack. It can also be seen that there is a sudden jump of $\bar{C}_p$ at $\alpha = 25^\circ$, separating the variation of $\bar{C}_p$ to two branches, one for $\alpha < 25^\circ$ and another for $\alpha > 25^\circ$. Also, at this angle of attack, the large confidence levels of $\bar{C}_p$ indicate the large temporal variation of the mean pressure coefficients. This implies that the pressure coefficients at this angle of attack are unsteady (non-stationary). For illustration of the unsteadiness, Figure 12 shows a time history of the pressure coefficient $C_p(t)$ for $\mathrm{Re} = 51\,000$ and $\alpha = 25^\circ$. As can be seen, there is unsteady behaviour in the time history of $C_p(t)$, resulting in two mean values, an upper mean and a lower mean which are represented by the green and red lines, respectively. The two states are more easily distinguished for higher Reynolds number of 51000 and 63000 than for lower Reynolds numbers of 25000 and 38000. The upper and lower means $\bar{C}_p$ for different Reynolds numbers are re-plotted in Figure 11 with the square and diamond markers, respectively. For the visualisation purpose that avoids the circle, square and diamond markers overlapping at $\alpha = 25^\circ$, the upper and lower means are plotted at $\alpha = 27^\circ$ instead of $\alpha = 25^\circ$.

It can be also seen from Figure 11 that, except for the upper means for $\mathrm{Re} = 25\,000$ and $38\,000$, the upper and lower means of $\bar{C}_p$ follow the pattern of the two branches of $\bar{C}_p$ for $\alpha > 25^\circ$ and $\alpha < 25^\circ$, respectively. The upper means for $\mathrm{Re} = 25\,000$ and $38\,000$ are in between the two branches, implying a transition between the two branches, which results from a flow switching

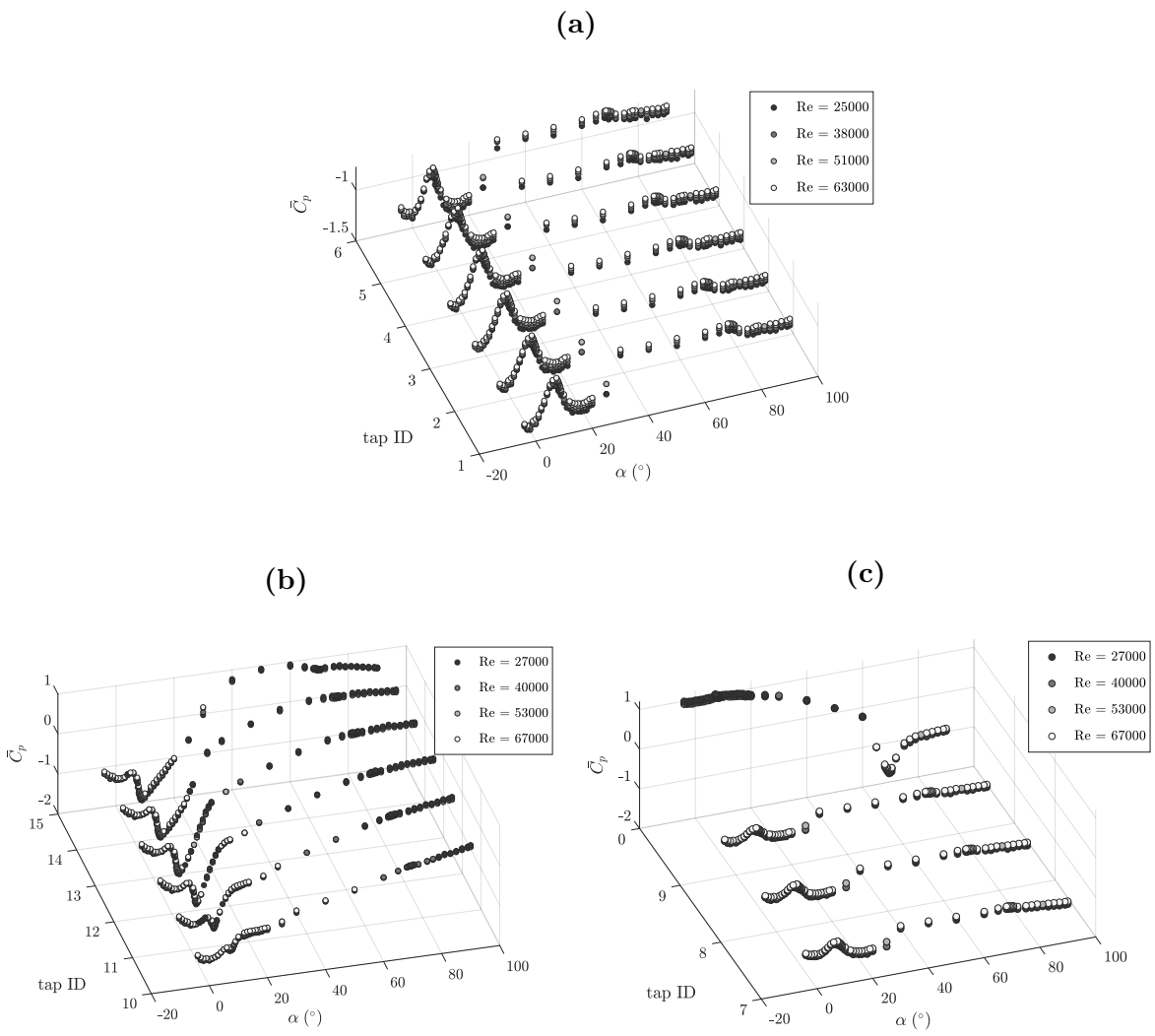

Figure 10: Mean pressure coefficients around sensor ring 1 for (a) pressure tap 1 to 6; (b) tap 10 to 15; (c) tap 0 and tap 7 to 9

from one state to another at this angle of attack. The switching flow feature is discussed in Section 7.2. To the authors' knowledge, these observations have not been reported in previous studies for 3:2 rectangular cylinders.

The time history of $C_p(t)$ in Figure 12 not only shows the non-stationary features but also shows the non-Gaussian characteristics. To examine the Gaussianity of the pressure coefficient for different angles of attack, Figure 13 shows the boxplot of $C_p(t)$ for each tested angle of attack and Reynolds number. For each box plot, the 5^{th} percentile, 50^{th} percentile (median) and 95^{th} percentile are estimated. It can be seen that $C_p(t)$ is clearly non-Gaussian for angles of attack from 10° to 25°. Outside this range, $C_p(t)$ is Gaussian. The non-stationary and non-Gaussian features in smooth wind will have consequences for modelling the aerodynamic loads and pressures on structures and will be discussed in Section 8.

Finally, Figure 14 shows the distribution of median, maximum and minimum pressure coefficients for Re = 51 000 at various angles of attack. The blue dots with the numerical values are for median $\underline{C}_p$. The gray shaded areas indicate the maximum and minimum pressure coefficients. These measures are used instead of the common statistical measures such as mean and RMS values because of non-Gaussian features as discussed above. For $\alpha = 0°$, the pressure on the front face (face C) is positive as expected, while the pressure on the other faces is negative (i.e. suction). Moreover, the pressure distributions on the top face (face A) and bottom face (face B) are almost symmetric, and the maximum suction on each face is at its trailing edge. As the angle of attack increases, the symmetry is lost. Also, whereas the distribution of the median pressures on the faces A and D changes only slightly, the distribution of pressure on face B changes significantly. Focusing on the pressure on face B, the suction tends to increase near the leading edge and decrease near the trailing edge as α increases from 0° to 8.3°. For higher and increasing angles of attack, the suction decreases and tends to positive pressure towards the leading edge. For α from about 70° to 90°, the suction disappears and the median pressure is positive across the whole of face B. From the pressure distributions it is possible to infer certain flow field features, which will be discussed in the next section.

6 Identification of flow features

Previous studies on rectangular sections with various side ratios (Carassale et al., 2014; Bruno et al., 2014; Schewe, 2013; Prosser and Smith, 2012; Huang et al., 2010; Matsumoto et al., 1998; Norberg, 1993) have identified the location of stagnation, flow separation and flow reattachment points as important flow field features influencing the aerodynamic forces. For $\alpha = 0°$, the mean flow separates from the two leading edges, creating two symmetric shear layers. The stagnation point is at the middle of the front face (face C, see Figure 2). As α increases, the flow remains detached from face A (top) and face B (bottom) until the critical angle of attack, at which

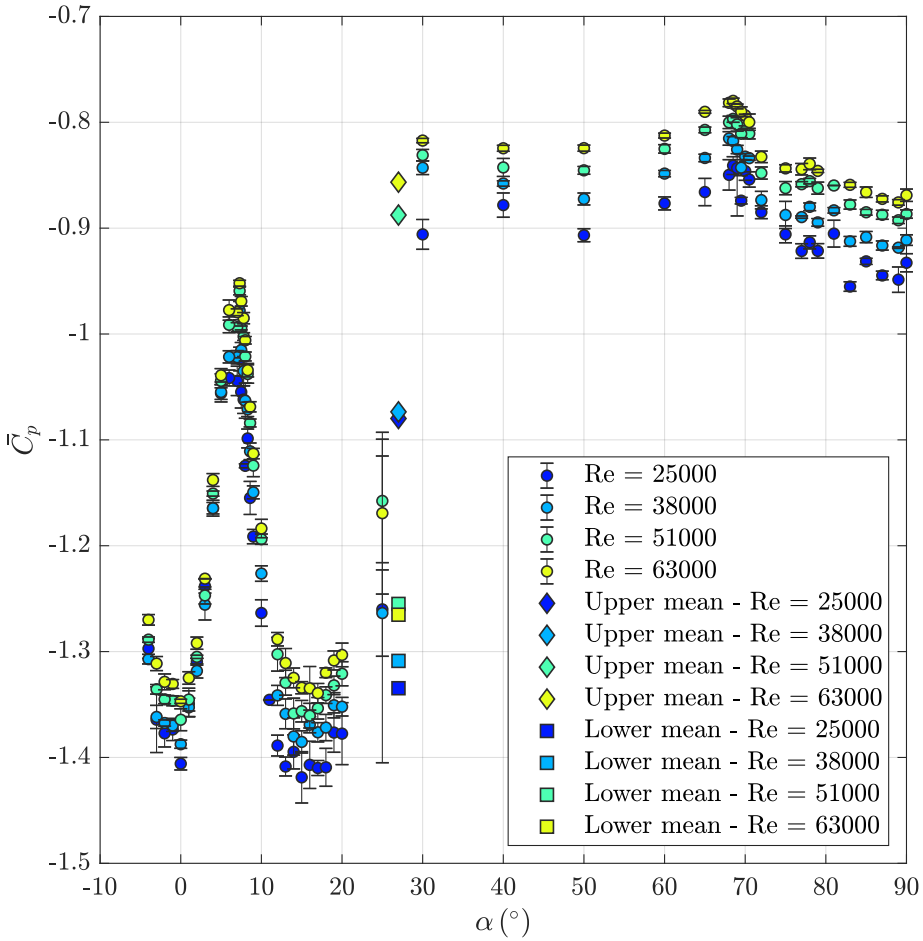

Figure 11: Variation of the mean pressure coefficients, $\bar{C}_p$, at tap 6. The upper and lower means are for $\alpha = 25°$

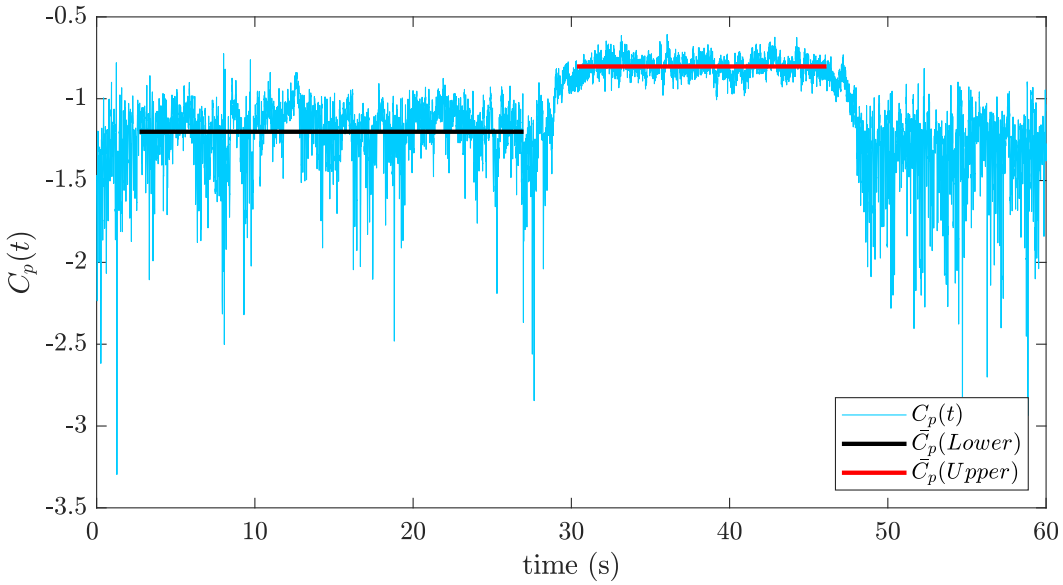

Figure 12: Time history of pressure coefficient at tap 6 for Re=51 000 and $\alpha = 25°$

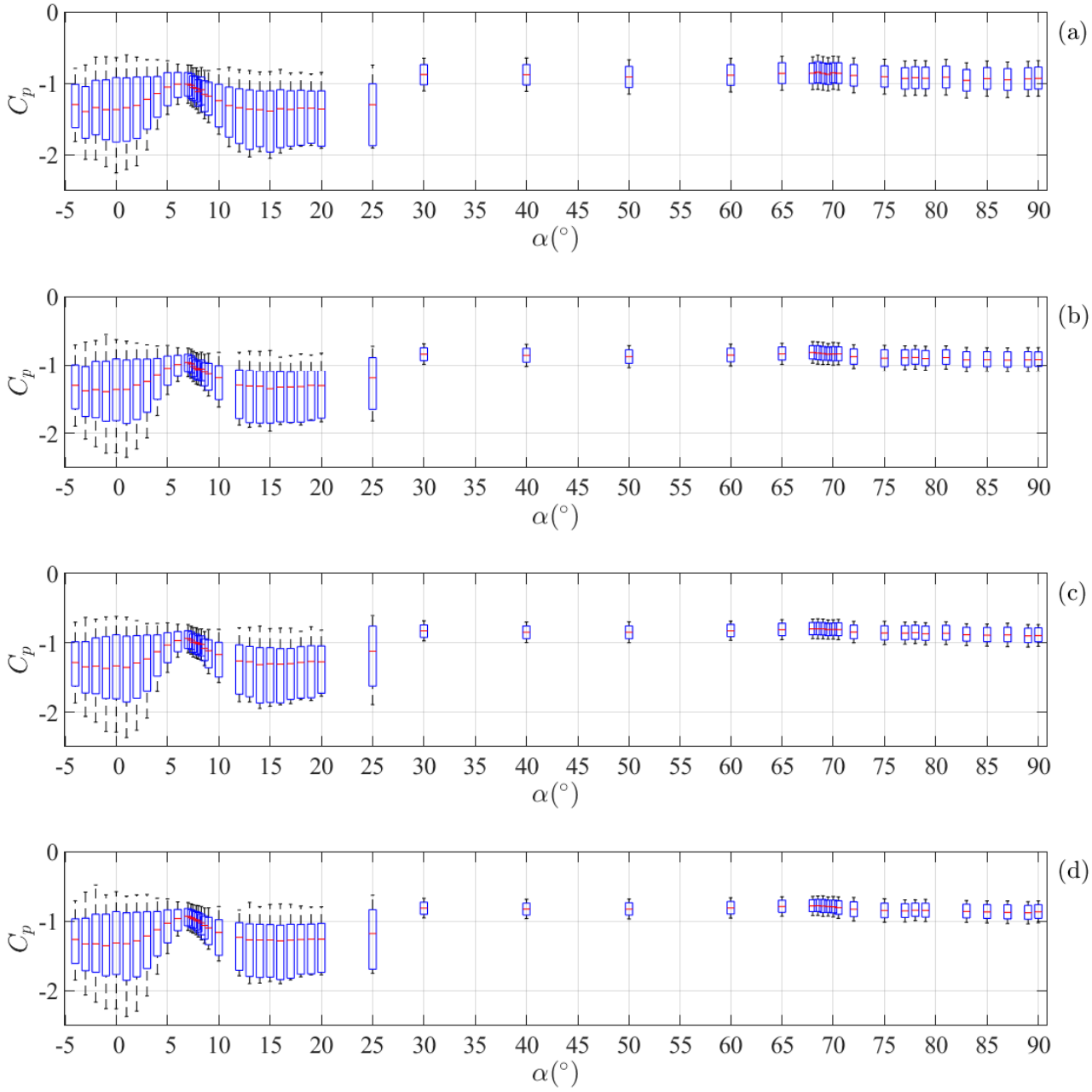

Figure 13: Variation of the statistical measures of $C_p(t)$ at tap 6: (a) Re = 25 000; (b) Re = 38 000; (c) Re = 51 000; and (d) Re = 63 000. For each box plot, median, 5^{th} percentile and 95^{th} percentile are estimated

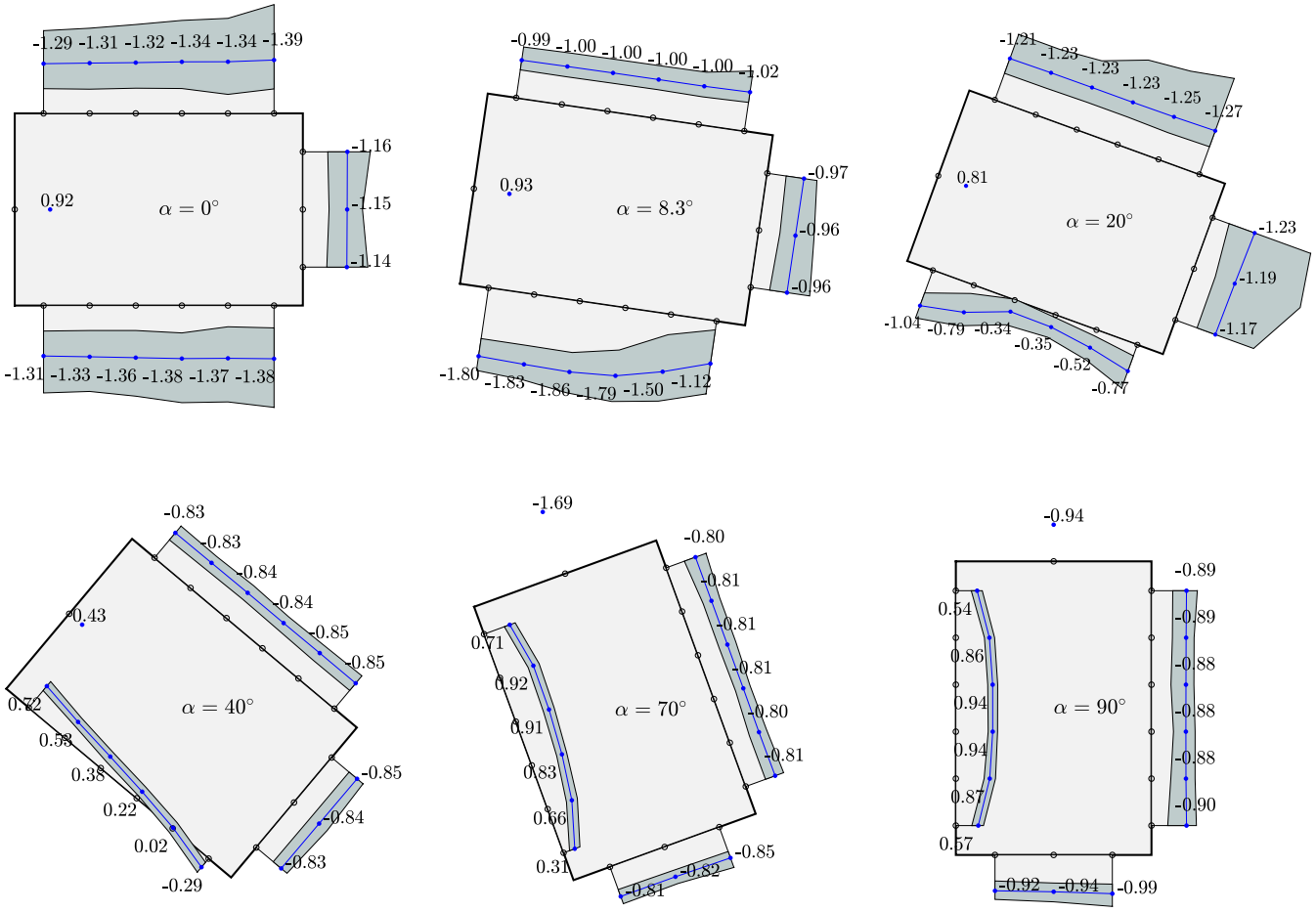

Figure 14: Distribution of the median pressure coefficient $\underline{C}_p$ (blue points with values) at each pressure tap for $\mathrm{Re} = 51\,000$. The shaded areas stand for maximum and minimum values of $C_p(t)$

reattachment first occurs on face B at a point near the trailing edge. This reattachment point moves towards the leading edge as α increases further, until at a high enough angle α the separation bubble disappears and the flow is fully attached on face B. At even higher angles of attack, the stagnation point moves from face C onto face B.

Given the importance of the stagnation, separation and reattachment points, it is noteworthy that these are not presented as functions of angle of attack in the literature, although a few studies determined such locations for specific angles of attack for certain rectangular sections. To address this limitation and better understand the flow features, flow separation and reattachment on face B are now considered through the analysis of the median pressures. The analysis is carried out for face B because, as discussed in Section 5, this is where significant changes of pressure distribution occur as α increases.

The locations of salient features at each angle of attack are identified by considering the positions of maxima in the pressure distributions. These are determined using a 4^{th}-order polynomial fit $f(s)$ to the median pressures $\underline{C}_p$ measured at the pressure taps on face B, where s is the coordinate measured from the corner of faces B and C. The fitting is illustrated in Figure 15 for $\alpha = 13°$ and $\alpha = 70°$ at Re=51 000. The position of each maximum is then estimated from the location where $f' = \mathrm{d}f(s)/\mathrm{d}s = 0$, in which d(.) stands for differentiating. Figure 16 shows the locations of the maxima obtained at different angles of attack.

Two sets of data are identified on Figure 16 and fitted using polynomial interpolations (continuous lines). Extrapolations of these polynomials are shown by dashed lines. For $\alpha = 25°$, the analysis is conducted for both the lower and upper regimes, which were discussed previously in Section 5. The first data set, indicated by triangle symbols, represents maxima where $\underline{C}_p \approx 1$. These correspond to stagnation points and air flows away from these along the surface of the section in both directions. These data show that at some value of α between 40° and 60°, the stagnation point moves from face C to face B. Extrapolation of the polynomial curve fit through the data points indicates this occurs at $\alpha \approx 52°$. Between $\alpha = 60°$ and $\alpha = 90°$, the stagnation point moves towards the centre of face B, so that when the section is orientated normal to the flow the stagnation point is at mid height, as expected.

The second data set, indicated by the square symbols, represents maxima where $\underline{C}_p < 1$. These maxima are first observed at the trailing edge ($s/B = 1$) for $\alpha = 8.4°$, which corresponds closely to the critical angle of attack observed in the variation of C_L and C_D. As α increases further, the location of the pressure maximum migrates across face B towards the leading edge. Extrapolation of the polynomial fit through these data indicates that the maximum would reach the leading edge at $\alpha \approx 38.4°$.

The meaning of these maxima is less clear than stagnation point discussed above, but they

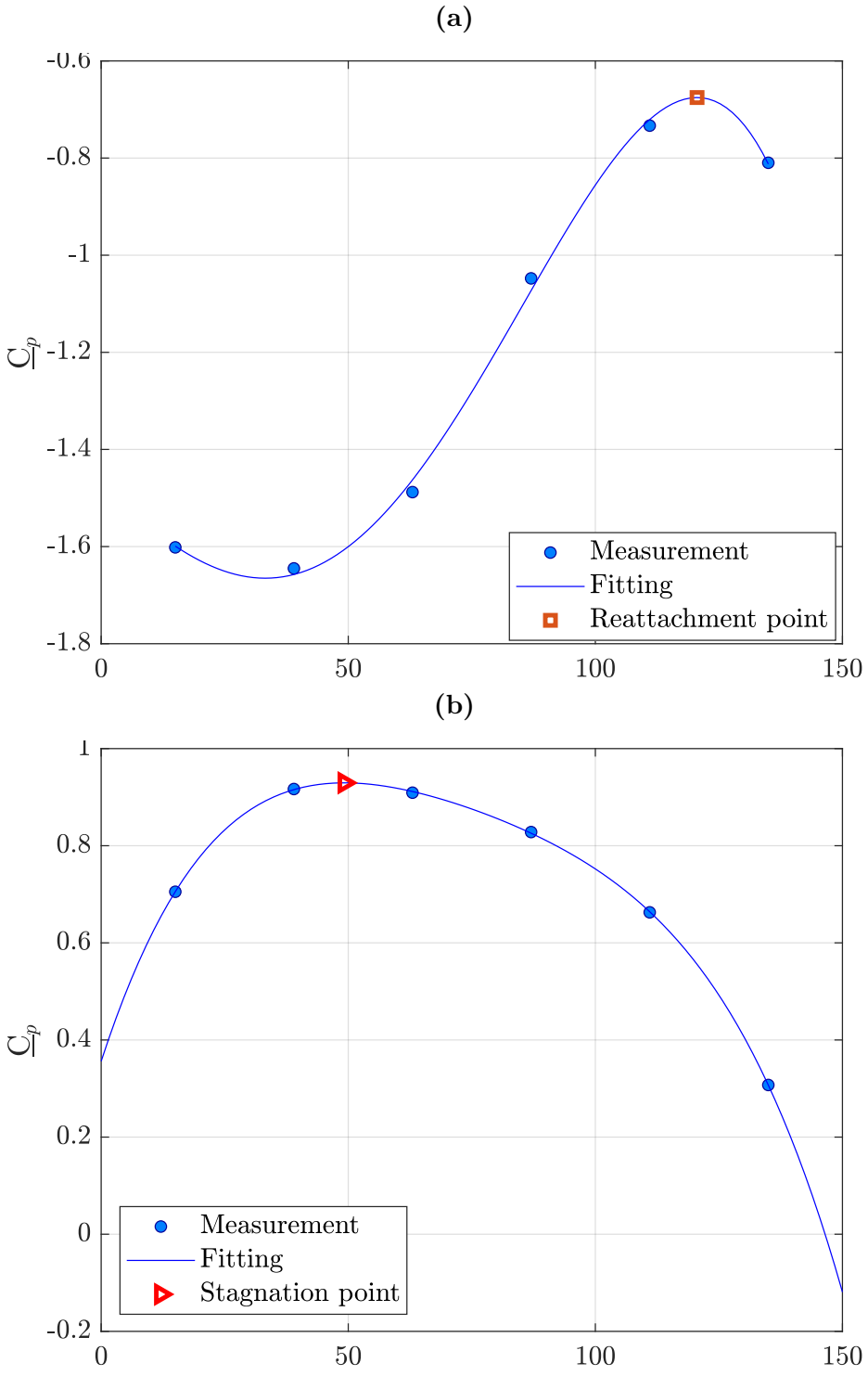

Figure 15: Illustration of curve fitting to identify (a) reattachment point ($\alpha = 13°$) and (b) stagnation point ($\alpha = 70°$) at Re=51 000

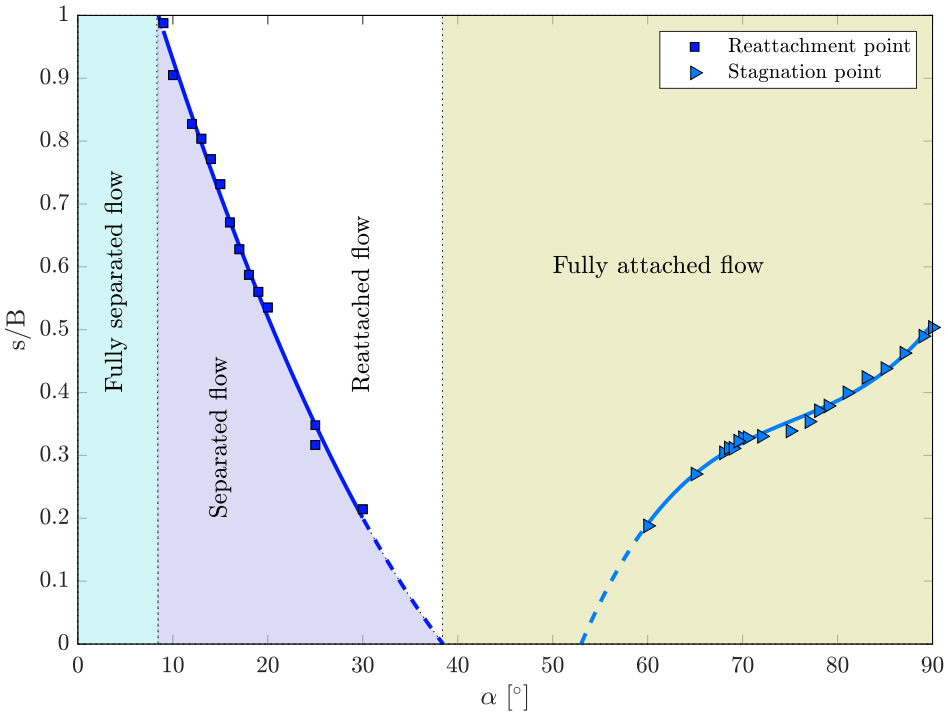

Figure 16: Characterised zones of flow features on Face B (Re= 51000). Continuous lines and dashed lines stand for interpolation and extrapolation fittings, respectively. s is the coordinate from the corner of face B and C (i.e. the leading edge of the bottom face as $\alpha = 0$)

can be interpreted as indicating possible flow reattachment in a similar way that a minimum in the pressure distribution can be used to identify possible flow separation. In this case, the observation that $f(s)$ is a maximum at the trailing edge of face B for $\alpha = 8.4°$ is consistent with observations in the literature that the critical value of α corresponds to reattachment at the trailing edge (Carassale et al., 2014; Huang et al., 2010; Norberg, 1993). The movement of the maxima of $f(s)$ towards the leading edge as α increases up to 38.4° then indicates that the re-circulation bubble associated with flow separation is getting smaller.

These two data sets enable four zones to be defined in Figure 16 as the angle of attack is varied. For α from 0° to 8.4°, the flow is fully separated from face A (top) and face B (bottom) and stays fully attached on face C (front face), shaded light green in Figure 16. For α from 8.4° to 38.4°, the maxima divide face B into two zones. The zone between the leading edge and the maximum point corresponds to $\underline{C}_p' > 0$, i.e. an adverse pressure gradient, which indicates a region of flow separation with a re-circulation bubble. This area is marked as the light purple zone in Figure 16. The zone between the maximum and the trailing edge corresponds $\underline{C}_p' < 0$, i.e. a favourable pressure gradient, and the flow reverses the direction, indicating the reattachment of the flow on the face. For α higher than 38.4°, $\underline{C}_p'$ is non-positive (see Figure 14 for some illustrative cases) and the flow is fully attached on face B. The zone of fully attached flow is coloured light yellow. The gradient $f'(s)$ is negative for α from 38.4° to 53°.

7 Analysis of non-stationary, non-Gaussian and switching flow features

The previous section explores the features of the separation and attachment of the flow as the angle of attack is changed. Vortex shedding is another important feature of the wind flow in bluff body aerodynamics. This has commonly been investigated by considering the PSD of the time series of lift force, pressure and velocity fluctuations in the wake. Such analysis is appropriate for stationary time series, however Sections 3 and 5 have shown that there are many angles of attack for which the aerodynamic forces and pressure are non-stationary. In such cases, the use of the PSD is no longer appropriate. Wavelet analysis is then a useful tool, because it enables time varying spectra to be captured for a non-stationary signal, for example $C_p(t)$ shown in Figure 12, which cannot be obtained using the classical Fourier transform or windowed Fourier transform (Perrier et al., 1995; Gurley and Kareem, 1999).

This section explores stationary and non-stationary features of the flow and whether the aerodynamic forces are Gaussian processes. The features are captured at the various angles of attack using Morlet wavelet analysis in addition to considering the PSD and probability density function (PDF) of the aerodynamic force and pressure. It was found that the features can be split into groups depending on whether α is smaller, equal to or higher than 25°. The switching flow at $\alpha = 25°$, which was inferred from Figure 3 and Figure 12, therefore marks an important transition in the non-stationary and non-Gaussian features observed. Section 7.1 discusses the steady vortex shedding for $\alpha < 25°$; Section 7.2 explores the switching phenomenon; and Section 7.3 investigates low-frequency vortices.

7.1 Steady vortex shedding for $\alpha < 25°$

For $\alpha = 0°$, the flow separates from the top and bottom leading edges, creating two symmetric shear layers that interact in the wake to form the Von Karman vortex street. These vortices are shed at a steady reduced frequency of $f^* = 0.11$, represented by a bright band in the wavelet map of $C_L(t)$, shown in the top left image of Figure 17. As α increases, the bright band is still prominent in the wavelet map, but is intermittent and less clear in the neighbourhood of $\alpha_{cr} \approx 8.3°$. This indicates that although vortex shedding is maintained in this region, the initial reattachment discussed in Section 6 is intermittent disturbing the formation of the vortex shedding and resulting in the blur in the vortex shedding band in the wavelet map.

As α is increased above 8.3° the vortex shedding band becomes more clearly defined, as shown in the lower right image of Figure 17 for $\alpha = 20°$. As discussed in Section 6, in this range of α the reattachment point on the bottom face moves away from the trailing edge towards the leading edge. The reattachment is therefore less intermittent and the vortex shedding is almost

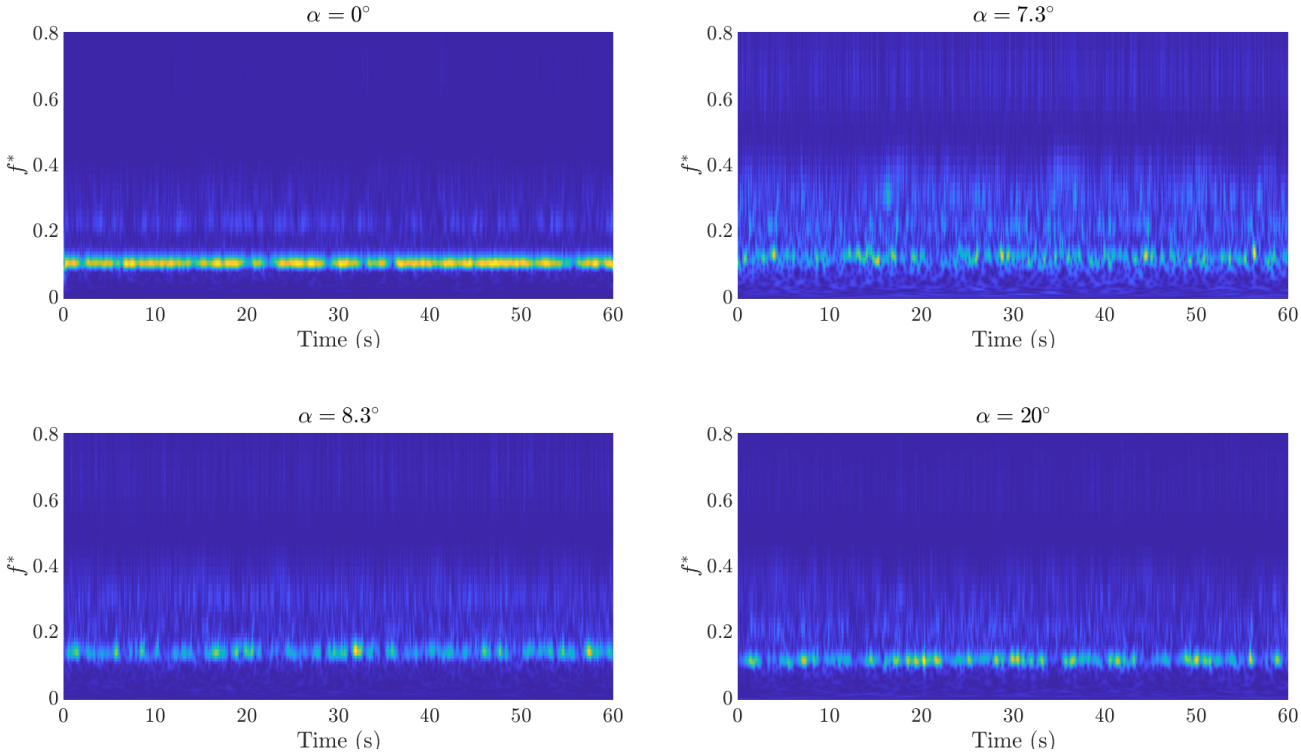

Figure 17: Wavelet map of $C_L(t)$ for Re=63 000 for various angles attack lower than 25°, where $f^* = fD/U$ is the reduced frequency

steady and occurs at a constant frequency.

7.2 Switching flow at $\alpha = 25°$

Figure 3 and Figure 12 have shown a jump in the time history of drag force and pressure for $\alpha = 25°$. This implies that the flow is strongly non-stationary, switching from one regime to the another. This switching flow phenomenon at $\alpha = 25°$ is now discussed further through the spectral, statistical and wavelet analyses of the lift force and pressure.

Figure 18a shows the PDF of the lower branch of $C_p(t)$ at tap 6 for Re = 51 000, which is re-plotted in Figure 18b. Figure 18c shows the PDF of the upper branch of $C_p(t)$. Figures 18d-f show the PSD of the lower branch of $C_p(t)$, time-frequency wavelet map of $C_p(t)$ and PSD of the upper branch of $C_p(t)$, respectively. For the lower branch of $C_p(t)$, the distribution of the pressure is non-Gaussian and there is a steady vortex shedding with a peak normalised frequency $f^* = 0.117$. The flow features appear to be generally similar to those for $\alpha < 25°$ discussed in Section 7.1.

As the flow switches to the regime in the upper branch of $C_p(t)$ (at a time of 27 seconds), the distribution of pressure becomes Gaussian (Figure 18c). However, a dominant frequency is not clear in the PSD or the wavelet map, although there is a blurred band corresponding to higher

frequency range from approximately 0.43 to 0.45. This implies low intensity vortex shedding at a mode higher than that of the Von Karman vortex street. There is a small peak at $f^* = 0.437$ in the PSDs for both flow regimes (Figure 18d-f).

Similar observations of the switching flow phenomenon are also found for other pressure taps and at other Reynolds numbers. The phenomenon can be inferred not only from the pressure, but also from the lift force, even though a jump is not seen in the force time history. This is most clearly illustrated through Figure 19, which presents the same analyses as Figure 18, but for $C_L(t)$.

It can be seen from Figure 19b and e that the same two regimes are observed for $C_L(t)$ with changes occurring at the same time as changes in the pressure data. The features of the PDF and PSD of each regime are similar to those of the pressure shown in Figure 18. The main difference between the two time histories is that there is no clear jump between the two regimes in the lift force. This will affect the distribution of the force and consequently the modelling of aerodynamic wind load. This issue is to be discussed in Section 8.

It is noted that although switching flow phenomena have previously been reported in the literature, the present study has identified some different features. Previously, the phenomenon has been observed from jumps in time history of lift force and pressure in critical Reynolds number range for the case of circular and elliptical cylinders (Schewe, 1986; Nikitas and Macdonald, 2015; Benidir et al., 2015; Ma et al., 2017). For square cylinders, most of the past studies (e.g. Norberg, 1993; Huang et al., 2010), have shown that the flow changes from one regime to another when α passes the critical value. Okajima (1982) presented a study for a B/D=3 rectangular section in which two vortex shedding modes, i.e. two Strouhal numbers, were evident at high Reynolds numbers, corresponding to two vortices on the back face. However, in that study there was no jump in the time history of velocity in the wake. So far, only the study by Carassale et al. (2014) has shown the existence of two flow regimes switching at a specific angle of attack. More specifically, that study was conducted for sharp and rounded square cylinders and found that the jump phenomenon was only observed from the lift force at the critical angle of attack and for rounded square sections. Moreover, the phenomenon at the critical angle of attack, was explained in terms of the intermittent reattachment leading to an unstable separation bubble on the bottom.

In the present study, the phenomenon has been observed in pressure, lift and drag data. Also, it has been seen to occur at a value of $\alpha = 25^\circ$ well above the critical angle of attack, where the separation bubble has already been formed. The origin of this phenomenon requires further investigation.

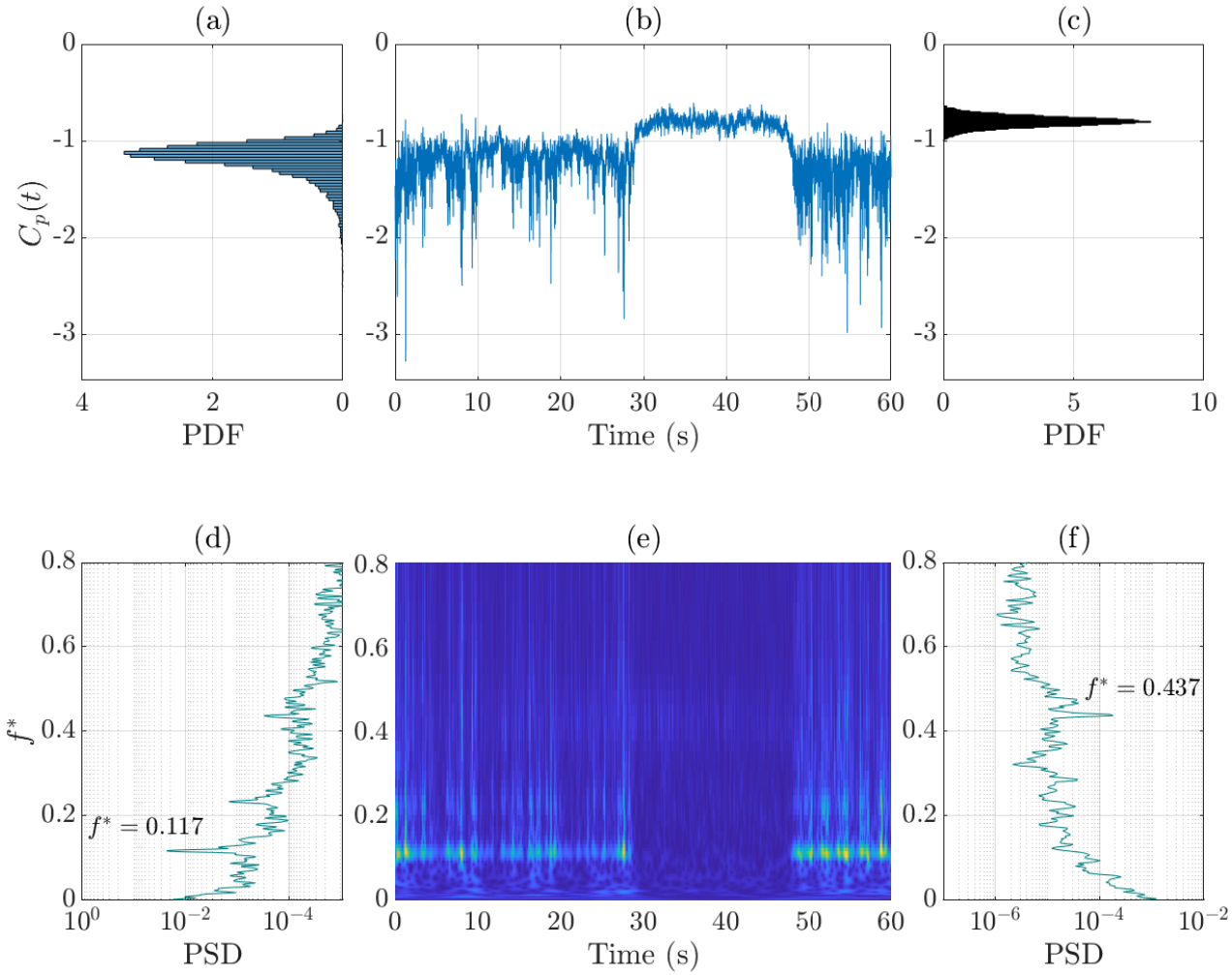

Figure 18: For pressure tap 6, Re = 51 000 and $\alpha = 25°$: (a) PDF of $C_p(t)$ for t=[5 s 25 s]; (b) Time history of $C_p(t)$; (c) PDF of $C_p(t)$ for t=[30 s 45 s]; (d) PSD of $C_p(t)$ for t=[5 s 25 s]; (e) Wavelet map of $C_p(t)$; (f) PSD of $C_p(t)$ for t=[30 s 45 s]

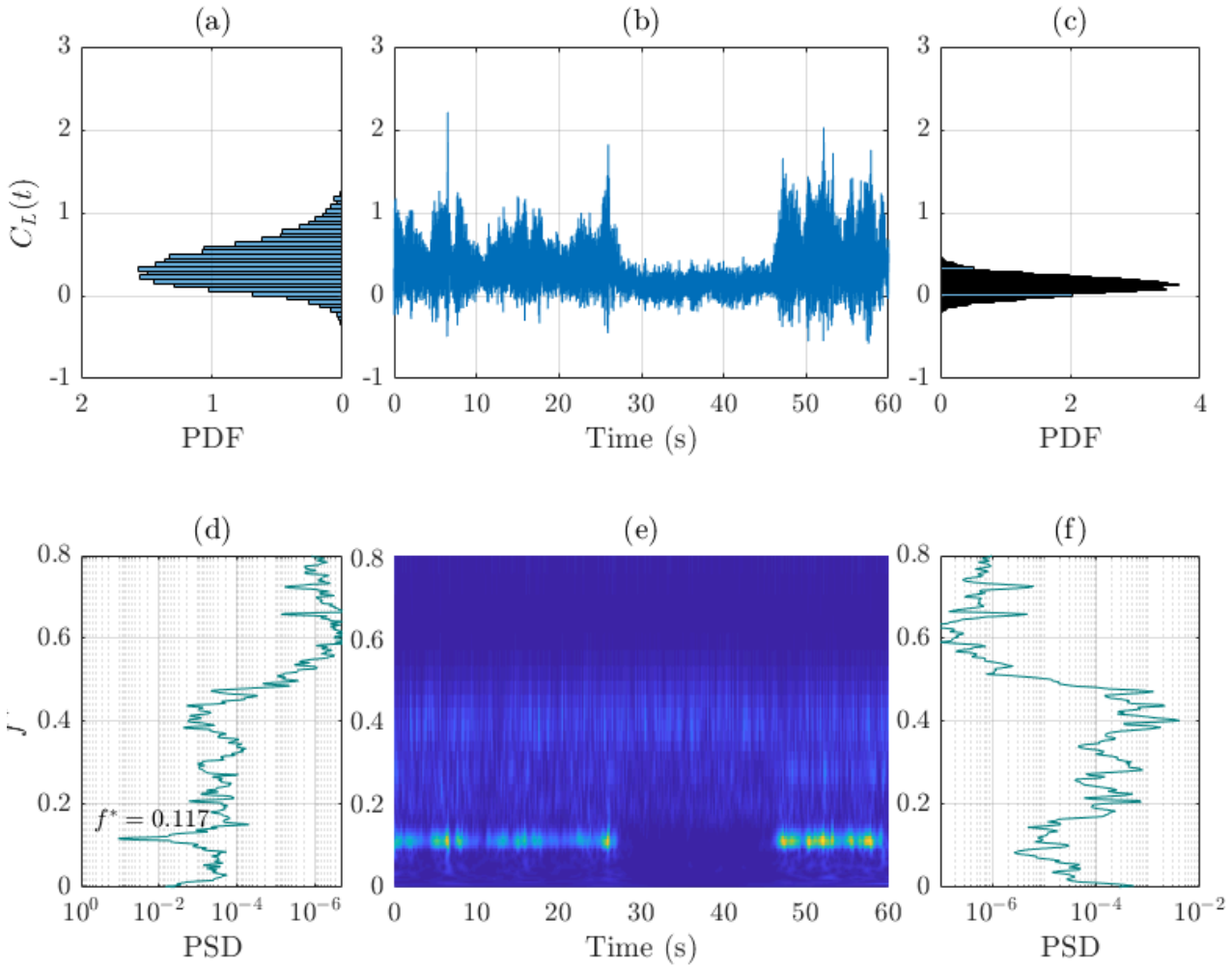

Figure 19: Lift coefficient, $C_L(t)$, for Re = 51 000 and $\alpha = 25°$: (a) PDF for t=[5 s 25 s]; (b) Time history; (c) PDF of $C_p(t)$ for t=[30 s 45 s]; (d) PSD for t=[5 s 25 s]; (e) Wavelet map; (f) PSD for t=[30 s 45 s]

7.3 Unsteady low frequency vortex shedding for $\alpha > 25^{\circ}$

Figure 20 shows the wavelet maps of the lift coefficient $C_L(t)$ for Re = 51 000 and four angles of attack from $30^{\circ} - 90^{\circ}$ using the same colour scale as the previous wavelet figures. Comparing Figure 20 and Figure 19e, it can be noticed that the map for $\alpha > 25^{\circ}$ is similar to the map for upper regime flow at $\alpha = 25^{\circ}$. More specifically, Von Karman vortex shedding cannot be identified and the blurred bands imply higher mode vortices. Furthermore, it was difficult to detect from the PSD of $C_L(t)$ at $\alpha > 25^{\circ}$ for higher Reynolds numbers, which is why, for $\alpha > 25^{\circ}$, Strouhal number is only shown for the lower Reynolds number in Figure 9.

To capture further features of the flow for $\alpha > 25^{\circ}$, Figure 21 shows the wavelet maps of $C_L(t)$ for $\alpha = 50^{\circ}$ and different Reynolds numbers, for the normalised frequency range from 0 to 0.12 with a smaller colour scale. Bright green zones are visible, implying unsteady vortices at frequencies much lower than the Von Karman vortex. Their normalised frequencies f^* are lower for higher Reynolds numbers. In particular, $f^* = 0.054 - 0.068$ (i.e. $f = 2.052 - 2.584$ Hz) for Re = 25 000; $f^* = 0.034 - 0.042$ (i.e. $f = 1.938 - 2.394$ Hz) for Re=38 000; $f^* = 0.025 - 0.034$ (i.e. $f = 1.9 - 2.584$ Hz) for Re = 51 000; $f^* = 0.015 - 0.024$ (i.e. $f = 1.425 - 2.28$ Hz) for Re = 63 000. Similar observations of unsteady low frequency vortex (LFV) can be found for other angles of attack $\alpha > 25^{\circ}$.

The unsteady LFV has been previously reported through experimental and computational investigations, specifically for normal plates and circular and trapezoidal cylinders (Szepessy and Bearman, 1992; Roshko, 1993; Najjar and Balachandar, 1998; Miau et al., 1999; Wu et al., 2005; Lehmkuhl et al., 2013; Sarwar and Mellibovskya, 2020). However, little information of the phenomenon is found for rectangular sections, except for the case of a square section presented by Cao and Tamura (2020). Moreover, the underlying physical mechanism has not yet been clearly described in the literature.

Szepessy and Bearman (1992); Roshko (1993) proposed that LFV is associated with the three-dimensional flow and coherence of span-wise vortices. Najjar and Balachandar (1998); Wu et al. (2005); Lehmkuhl et al. (2013) explained that the LFV is resulted from the existence of two flow regimes, one corresponds to high mean drag with high coherence in the span-wise vortices and another corresponds to low mean drag with less coherent vortices. Miau et al. (1999); Lehmkuhl et al. (2013) showed that the unsteady variation of the vortex formation length is responsible for the occurrence of the phenomenon. One common finding is that Reynolds number has a significant effect on the formation of LFV.

It is worth noting that much of the work in the literature used the Fourier transform to identify the LFV through the PSD of, for example, lift force. As mentioned earlier, this method is not appropriate for unsteady flow. Therefore, previous findings with the quantitative measures of

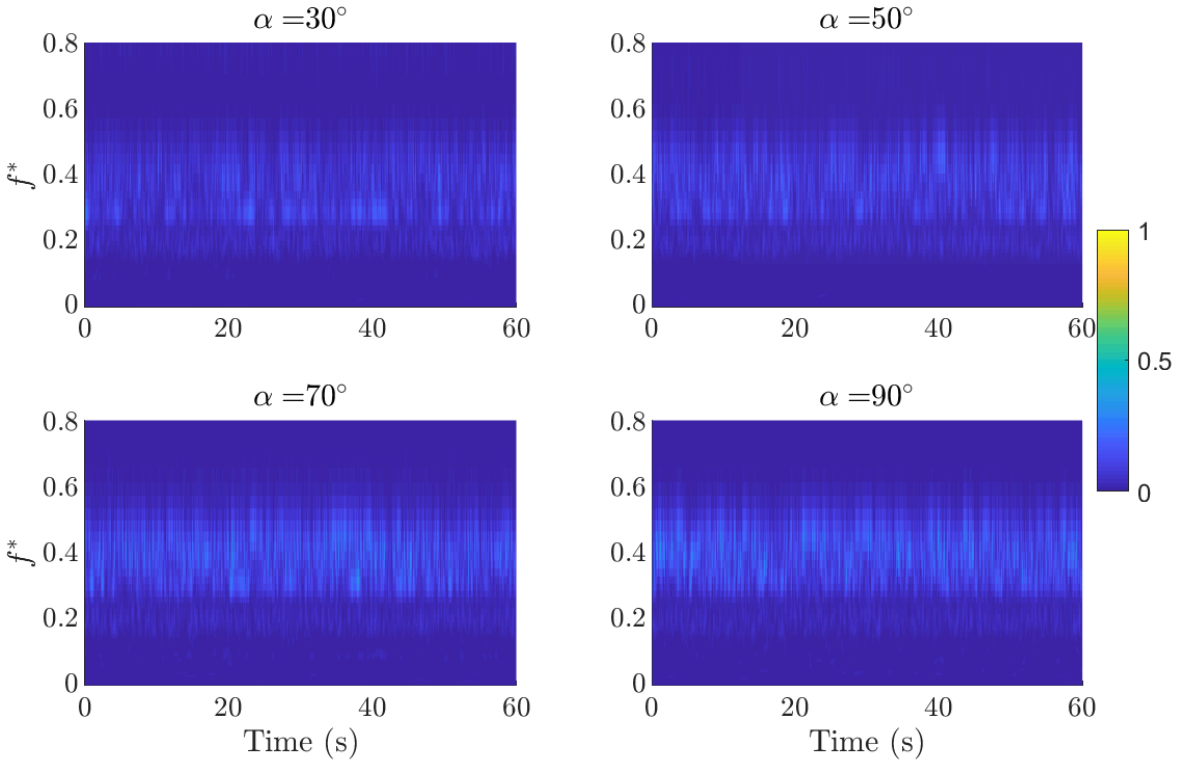

Figure 20: Wavelet map of $C_L(t)$ for Re = 51 000 and for various values of α

LFV may be not precise.

8 Discussion on the non-Gaussian and non-stationary features

An important consequence of the non-stationary and non-Gaussian features noted above pertains to the estimation of wind loads. Wind loading codes and standards seek to provide estimates of extreme loads on structures. These are typically based on a given probability of occurrence that reflects both the uncertainty in the wind speed for a given site and the uncertainty of the pressure and force coefficients. For example, the EuroCode (EN1991-1-4, 2005) specifies the characteristic value of the wind speed as a 10 minute mean with an annual probability of exceedence of 0.02 and requires that values of force and pressure coefficients are chosen to maintain the same overall probability of occurrence for the wind loads on the structure. This represents a development of the so-called Cook-Mayne method (Cook and Mayne, 1979, 1980). Clearly, the estimation of appropriate extreme values for pressure and force coefficients will be influenced by whether or not the data are stationary and Gaussian. In the literature, several methods have been proposed to estimate extreme values of non-Gaussian wind pressure (Kumar and Stathopoulos, 2000; Holmes and Cochran, 2003; Kwon and Kareem, 2011; Ding and Chen, 2014; Yang and Tian, 2015; Yang et al., 2019). In the present study, it has been shown earlier that non-Gaussian wind forces and pressure are found (e.g. see Figure 13). Therefore, the

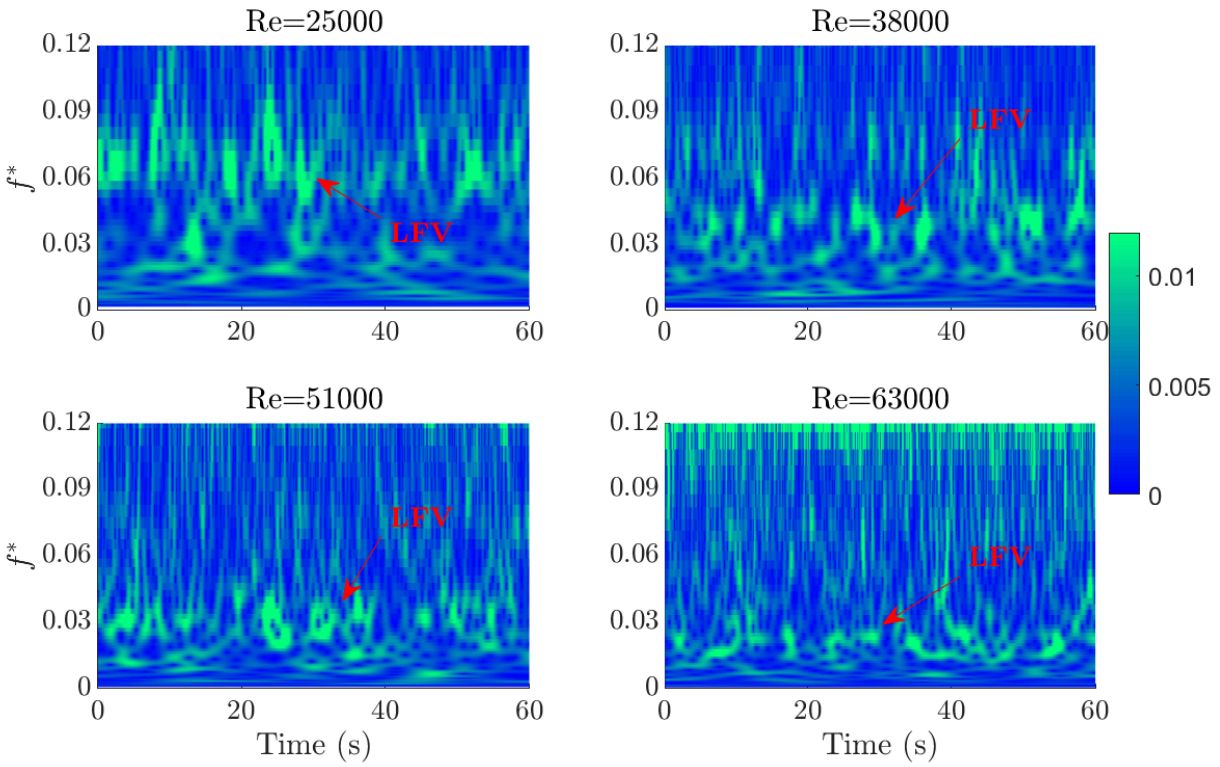

Figure 21: Wavelet map of $C_L(t)$ for $\alpha = 50°$: Low frequency vortex (LFV) appearance

median and quantiles are more appropriate statistical measures than the mean and standard deviation. Figure 22(a) and (b) compares the mean pressure $\bar{C}_p$ and median pressure $\underline{C}_p$ and their relative difference for C_p at tap 6 for Re=51 000. Figure 23 is similar to Figure 22 but shows $\bar{C}_p + \tilde{C}_p$ (i.e. mean plus standard deviation of $C_p(t)$) and 84.13^{th} percentile of $C_p(t)$ (denoted that $C_{p,84.13}$). It is noted that $\underline{C}_p$ and $C_{p,84.13}$ become $\bar{C}_p$ and $\bar{C}_p + \tilde{C}_p$, respectively, for Gaussian data. The case for $\alpha = 25°$ is excluded from the figures and discussed later.

It can be seen that the non-Gaussian distribution of the data has most influence for $\alpha = 0° - 20°$ and that for $\alpha = 30° - 90°$ there is negligible difference between the two sets of statistics. The difference between $\bar{C}_p$ and $\underline{C}_p$ is most significant for $\alpha = 10° - 20°$, whereas the difference between $\bar{C}_p + \tilde{C}_p$ and $C_{p,84.13}$ for α in the region of 0°. It should also be noted that there is no difference in the two sets of statistics at the critical angle of attack.

Therefore, the accurate estimation of extreme values from wind tunnel tests requires appropriate centiles of pressure and force coefficients to be found. For unimodal data, this influences the amount of data that needs to be collected from wind tunnel tests. However, for the switching flow described earlier for $\alpha = 25°$ the data might be bimodal. Figure 24a-d show respectively the PDF of $C_D(t)$, $C_L(t)$, $C_M(t)$ and $C_p(t)$ (at tap 6) for Re = 51 000 and $\alpha = 25°$. The distributions of $C_D(t)$ and $C_p(t)$ are clearly bimodal, whereas the distributions of $C_L(t)$ and $C_M(t)$ are unimodal. Although a few studies in the literature reported the bimodal distribution of wind pressure (Hui et al., 2013; Chen et al., 2020), discussion on its impact modelling of on

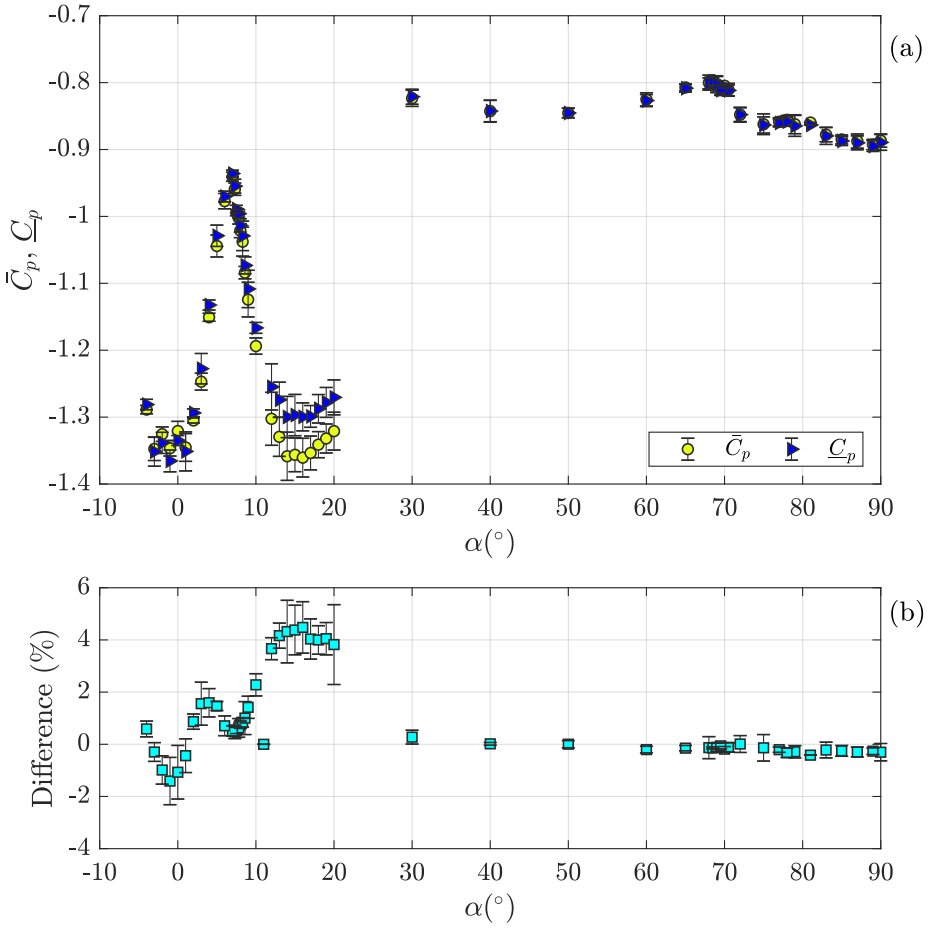

Figure 22: For pressure tap 6 and Re = 51 000: Comparison between mean pressure coefficient ($\bar{C}_p$) and median pressure coefficient ($\underline{C}_p$) (a) and their relative difference (b).

wind loading and pressure is limited. The nature of the bimodal distribution will depend on the proportion of time spent in each flow regime, which is difficult to predict given the unsteady nature of the phenomenon. It is therefore important to investigate this topic further.

Finally, it is noted that non-stationarity and non-Gaussianity raise serious questions on the use of quasi-steady force coefficients. For example, when quasi-steady theory is adopted to predict the onset of galloping, use is made of the factor $\bar{C}_D + \bar{C}'_L$, where $\bar{C}'_L$ is the derivative of $\bar{C}_L$ with respect to α. For values of α that result in switching flow, the bimodal distribution of $C_D(t)$ leads to two different values of $\bar{C}_D + \bar{C}'_L$, associated with the two flow regimes. However, predictions based on an average value of C_D will not correspond to either flow regime and so the likelihood of galloping will not be represented correctly. In addition, the non-stationarity and non-Gaussianity shown above might be changed for vibrating structures, which might contribute to the amplitude-dependence of aerodynamic forces and flow field features (e.g. Lin et al., 2019). Therefore, the influence of switching flow on the likelihood of non-linear aeroelastic responses is another topic worthy of further investigation.

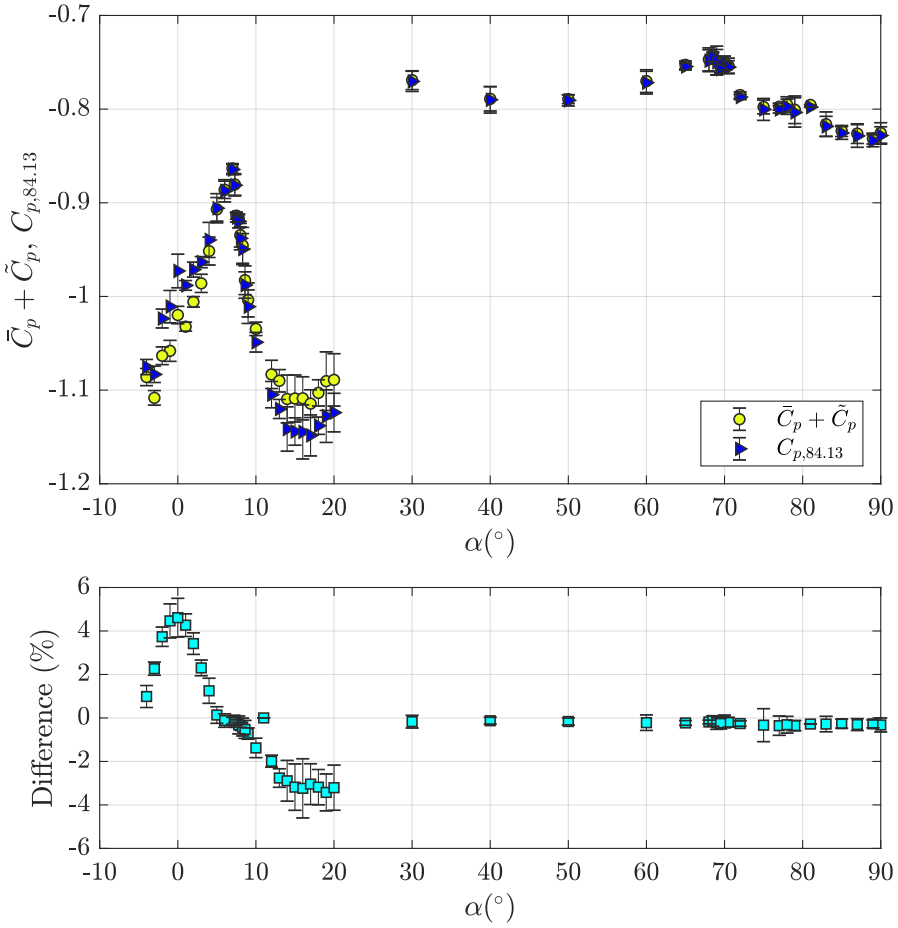

Figure 23: Comparison between $\bar{C}_p + \tilde{C}_p$ and 84.13$^{\text{th}}$ percentile of $C_p(t)$ at tap 6 for $\text{Re} = 51\,000$.

9 Conclusions

This paper has presented further insights into the aerodynamic behaviour of rectangular cylinders through a series of wind tunnel tests on a static 3:2 rectangular prism in smooth flow for a wide range of angles of attack from -4° to 90° and four values of Reynolds number from 25 000 to 63 000. The aerodynamic forces and surface pressure distribution were measured and analysed to determine their characteristics and infer flow field features. The following conclusions are drawn.

First, the mean lift and moment coefficients are almost independent of Reynolds number, whereas the mean drag coefficients are dependent on Reynolds number. The RMS of the fluctuations of drag and lift coefficients are dependent on Reynolds number for angles of attack smaller than 30°. For angles of attack between 30° and 90°, the fluctuations of lift and drag coefficients are smaller than 0.1 and are almost independent on Reynolds number. The RMS of the moment coefficients are dependent on Reynolds number, but both the RMS and mean of the moment coefficients have small absolute values (both are smaller than 0.15). The observed dependence of Reynolds number is in contrast to findings in the literature that mean coefficients are independent of Reynolds number. However, the data in the literature is limited to drag and lift coefficients for angles of attack between -4° and 16°.

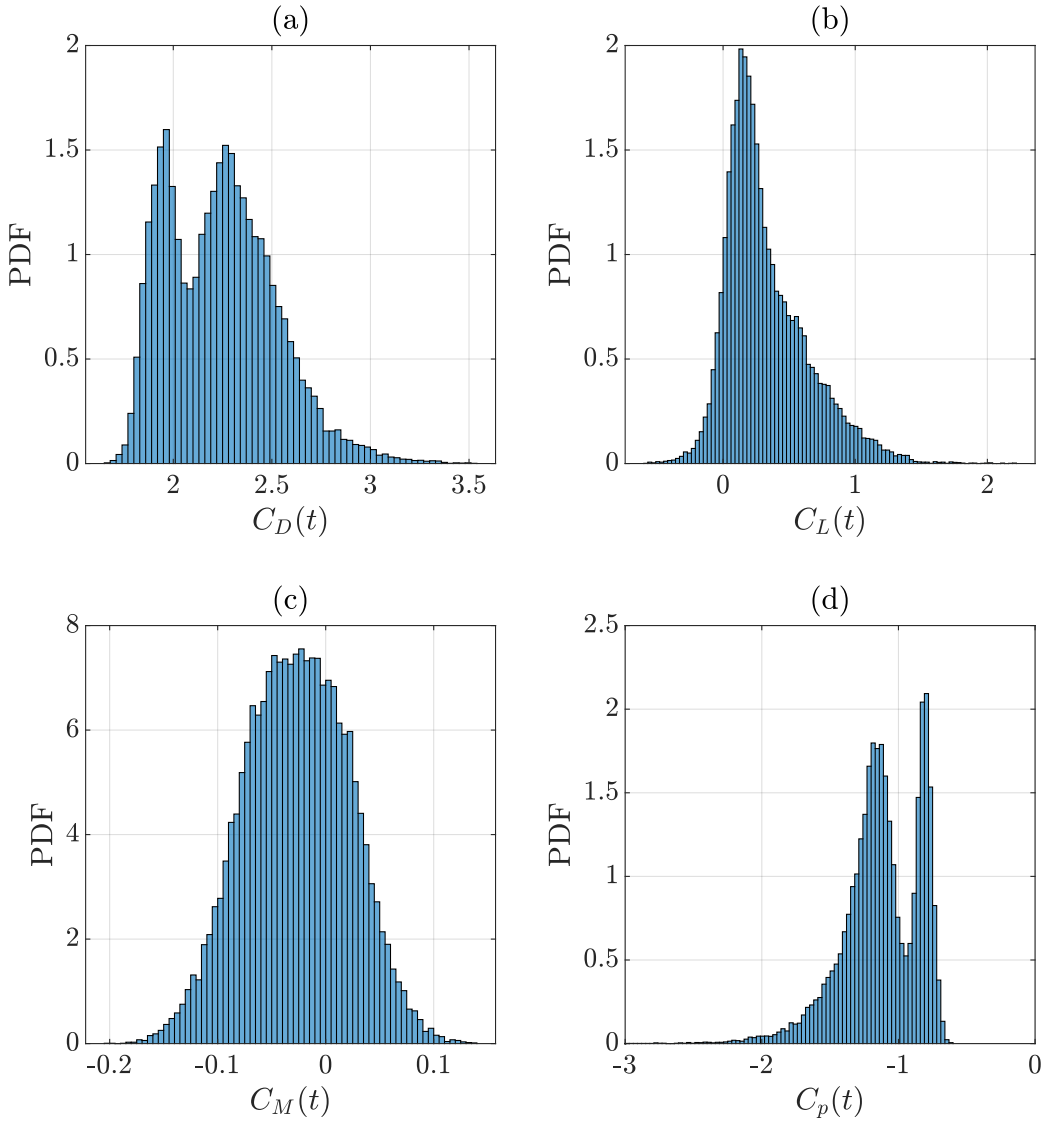

Figure 24: For Re = 51 000 and $\alpha = 25°$, probability distribution of (a) $C_D(t)$; (b) $C_L(t)$; (c) $C_M(t)$; (d) $C_p(t)$ at tap 6.

Second, the critical angle of attack based on minimum peaks in mean drag and lift coefficients occurs at $\alpha \approx 8.3^\circ$, which agrees reasonably well with previous studies on 3:2 rectangular cylinders, i.e. 7° in water tank experiments for Re $< 10\,000$ by Massai et al. (2018) and 9° in wind tunnel experiments for Re $= 143\,000$ by Mannini et al. (2018). However, the present study found that the minimum peaks of the means of drag, lift, moment and pressure coefficients and the maximum peak of Strouhal number do not occur at the same angle of attack. The peak values for the mean moment coefficients, mean pressure coefficients and Strouhal number are at $\alpha \approx 11^\circ$, $\alpha \approx 7.3^\circ$ and $\alpha \approx 9^\circ$, respectively. A second critical angle of attack was observed at $\alpha \approx 70^\circ$, which corresponds to the 2:3 rectangular section.

Third, the study presented a map to identify the locations of the reattachment and stagnation points on the lower face (face B) with variation of angle of attack. The map also shows the ranges of angle of attack where the flow is fully or partially separated and fully or partially attached on the face. The map is helpful to understand how the flow behaves around the body. More specifically, the flow is fully separated from the lower face for $\alpha = 0^\circ - 8.4^\circ$ and fully attached to the lower face for $\alpha = 38.4^\circ - 90^\circ$. In between these ranges, the flow separates from the leading edge and reattaches part way along the face.

Fourth, for $\alpha = 25^\circ$, clear jumps are seen in the time histories of the drag force and pressure coefficients, but not for the lift force and moment. To the authors' knowledge, this jump phenomenon has not been reported before for rectangular sections, although a similar phenomenon was previously observed in the lift force of a rounded square section (but at the critical angle of attack) and in the lift force of circular and elliptical sections in the critical Reynolds number range. The jumps result in bi-modal distributions of drag force and pressure. This observation is explained in terms of the flow switching between two different regimes.

Fifth, the switching flow observed at $\alpha = 25^\circ$ results in non-stationary time histories for the drag and pressure coefficients. At this angle of attack the two flow regimes separate the features of vortex shedding into two categories. The flow corresponding to the first regime at $\alpha = 25^\circ$ and the flow for $\alpha < 25^\circ$ are similar to steady Von Karman vortex shedding. The flow corresponding to the second regime for $\alpha = 25^\circ$ and the flow for $\alpha > 25^\circ$ similar features to unsteady low-frequency vortex shedding; Von Karman vortex shedding cannot be identified from the lift force and pressure. There is little information on low-frequency vortex shedding in the literature for rectangular cylinders and this phenomenon is absent from current codes of practice.

Finally, it is highlighted that accurate prediction of design wind forces and pressures on structures requires that non-Gaussian, non-stationary and bi-modal features should be accounted for if they are present in the force and pressure coefficient data. Similarly, predictions of the critical wind speed for galloping should account for non-stationarity in the force coefficient data.

Studies on the dynamic response of the section have also been performed and will be presented in a future paper. Further work is required to determine better the importance of the non-stationary and non-Gaussian data observed here and to investigate the amplitude dependence of the aero-elastic response.

10 Acknowledgements

This research is funded through the International Collaboration Award of the Global Challenge Research Fund (GCRF) delivered by the UK Royal Society, reference number IC170137, for the project "Improving the Resilience of Infrastructure in Storms (IRIS)".

The authors would like to thank Dr Tommaso Massai from University of Florence for sharing the data and discussion on Strouhal number of a 3:2 section.

References

A. J. Álvarez, F. Nieto, D. T. Nguyen, J. S. Owen, and S. Hernández. 3D LES simulations of a static and vertically free-to-oscillate 4:1 rectangular cylinder: Effects of the grid resolution. *Journal of Wind Engineering and Industrial Aerodynamics*, 192:31–44, 2019. doi: 10.1016/j.jweia.2019.06.012.

A. Benidir, O. Flamand, L. Gaillet, and D. G. Impact of roughness and circularity-defect on bridge cables stability. *Journal of Wind Engineering and Industrial Aerodynamics*, 137:1–13, 2015. doi: 10.1016/j.jweia.2014.11.010.

L. Bruno, M. V. Salvetti, and F. Ricciardelli. Benchmark on the aerodynamics of a rectangular 5:1 cylinder: An overview after the first four years of activity. *Journal of Wind Engineering and Industrial Aerodynamics*, 126:87–106, 2014. doi: 10.1016/j.jweia.2014.01.005.

Y. Cao and T. Tamura. Low-frequency unsteadiness in the flow around a square cylinder with critical angle of 14° at the Reynolds number of 2.2×10^4. *Journal of Wind Engineering and Industrial Aerodynamics*, 97, 2020.

L. Carassale, A. Freda, and M. Marrè-Brunenghi. Experimental investigation on the aerodynamic behavior of square cylinders with rounded corners. *Journal of Fluids and Structures*, 44:195–204, 2014. doi: 10.1016/j.jfluidstructs.2013.10.010.

Y. Chen, K. Djidjeli, and Z.-T. Xie. Large eddy simulation of flow past stationary and oscillating square cylinders. *Journal of Fluids and Structures*, 97, 2020.

N. Cook and J. Mayne. Aerodynamic effects of the angle of attack on a rectangular prism. *Journal of Wind Engineering and Industrial Aerodynamics*, 4:149—-164, 1979.

N. Cook and J. Mayne. A refined working approach to the assessment of wind loads for equivalent static design. *Journal of Wind Engineering and Industrial Aerodynamics*, 6:125–137, 1980.

Demartino, C. and Ricciardelli, F. Aerodynamics of nominally circular cylinders: A review of experimental results for Civil Engineering applications. *Engineering Structures*, 137, 2017.

J. Ding and X. Chen. Assessment of methods for extreme value analysis of non-Gaussian wind effects with short-term time history samples. *Engineering Structures*, 80:75–88, 2014.

S. Dutta, K. Muralidhar, and P. Panigrahi. Experimental study of flow past a square cylinder at high Reynolds numbers. *Experiments in Fluids*, 34, 2003.

EN1991-1-4. EN1991-1-4, Eurocode 1: Actions on structures - Part 1-4: General actions - Wind actions, 2005.

K. Gurley and A. Kareem. Applications of wavelet transforms in earthquake, wind and ocean engineering. *Engineering Structures*, 21:149–167, 1999.

J. Holmes and L. Cochran. Probability distributions of extreme pressure coefficients. *Journal of Wind Engineering and Industrial Aerodynamics*, 91:893–901, 2003.

J. D. Holmes and T. K. Tse. International high-frequency base balance benchmark study. *Wind and Structures, An International Journal*, 18(4):457–471, 2014. doi: 10.12989/was.2014.18.4.457.

R. F. Huang, B. H. Lin, and S. C. Yen. Time-averaged topological flow patterns and their influence on vortex shedding of a square cylinder in crossflow at incidence. *Journal of Fluids and Structures*, 26(3):406–429, 2010. doi: 10.1016/j.jfluidstructs.2010.01.003.

Y. Hui, A. Yoshida, and Y. Tamura. Interference effects between two rectangular-section high-rise buildings on local peak pressure coefficients. *Journal of Fluids and Structures*, 37: 120–133, 2013.

T. Igarashi. Characteristics of the flow around a square prism. *Bulletin of JSME*, 27, 1984.

Y. Ito, H. Shirato, and M. Matsumoto. Coherence functions of fluctuating lift forces for bridge decks. *Journal of Wind Engineering and Industrial Aerodynamics*, pages 1–9, 2015.

C. W. Knisely. Strouhal numbers of rectangular cylinders at incidence: A review and new data. *Journal of Fluids and Structures*, 4:371–393, 1990.

K. Kumar and T. Stathopoulos. Wind loads on low building roofs: a stochastic perspective. *Journal of Structure Engineering*, 126:944–956, 2000.

D. Kwon and A. Kareem. Peak factors for non-Gaussian load effects revisited. *Journal of Structure Engineering*, 137:1611–1619, 2011.

B. E. Lee. The effect of turbulence on the surface pressure field of a square prism. *Journal of Fluid Mechanics*, 69:263–282, 1975.

O. Lehmkuhl, I. Rodriguez, R. Borrell, and A. Oliva. Low-frequency unsteadiness in the vortex formation region of a circular cylinder. *Physics of Fluids*, 25, 2013.

S. Lin, Q. Wang, N. Nikitas, and H. Liao. Effects of oscillation amplitude on motion-induced forces for 5:1 rectangular cylinders. *Journal of Wind Engineering and Industrial Aerodynamics*, 186, 2019.

S. Luo, X. Tong, and B. Khoo. Transition phenomena in the wake of a square cylinder. *Journal of Fluids and Structures*, 23, 2007.

W. Ma, J. H. G. Macdonald, Q. Liu, C. H. Nguyen, and X. Liu. Galloping of an elliptical cylinder at the critical Reynolds number and its quasi-steady prediction. *Journal of Wind Engineering and Industrial Aerodynamics*, 168:110–222, 2017. doi: 10.1016/j.jweia.2017.04.022.

C. Mannini, A. M. Marra, and G. Bartoli. VIV-galloping instability of rectangular cylinders: Review and new experiments. *Journal of Wind Engineering and Industrial Aerodynamics*, 132:109–124, 2014. doi: 10.1016/j.jweia.2014.06.021.

C. Mannini, T. Massai, and A. M. Marra. Unsteady galloping of a rectangular cylinder in turbulent flow. *Journal of Wind Engineering and Industrial Aerodynamics*, 173(November 2017):210–226, 2018. doi: 10.1016/j.jweia.2017.11.010.

T. Massai, J. Zhao, D. L. Jacono, G. Bartoli, and J. Sheridan. The effect of angle of attack on flow-induced vibration of low-side-ratio rectangular cylinders. *Journal of Fluids and Structures*, 82:375–393, 2018. doi: 10.1016/j.jfluidstructs.2018.07.011.

M. Matsumoto. Aerodynamic damping of prisms. *Journal of Wind Engineering and Industrial Aerodynamics*, 59:159–175, 1996. doi: 10.1016/0167-6105(96)00005-0.

M. Matsumoto, H. Ishizaki, C. Matsuoka, Y. Daito, Y. Ichikawa, and S. Shimahara. Aerodynamic effects of the angle of attack on a rectangular prism. *Journal of Wind Engineering and Industrial Aerodynamics*, 77-78:531–542, 1998.

J. Miau, J. Wang, C. J.H., and W. C.Y. Characteristics of low-frequency variations embedded in vortex shedding process. *Journal of Fluids and Structures*, 13:339–359, 1999. doi: 10.1006/jfls.1999.0206.

F. Najjar and S. Balachandar. Low-frequency unsteadiness in the wake of a normal flat plate. *Journal of Fluid Mechanics*, 370:101–147, 1998. doi: 10.1017/S0022112098002110.

C. H. Nguyen, J. H. G. Macdonald, and S. Cammelli. Non-across-wind galloping of a square-section cylinder. *Meccanica*, 55:1333–1345, 2020a. doi: 10.1007/s11012-020-01166-6.

C. H. Nguyen, J. S. Owen, J. Franke, L. C. Neves, and D. M. Hargreaves. Typhoon track

simulations in the North West Pacific: informing a new wind map for Vietnam. *Journal of Wind Engineering and Industrial Aerodynamics*, 2020b.

D. T. Nguyen, D. M. Hargreaves, and J. S. Owen. Vortex-induced vibration of a 5:1 rectangular cylinder: A comparison of wind tunnel sectional model tests and computational simulations. *Journal of Wind Engineering and Industrial Aerodynamics*, 175:1–16, 2018. doi: 10.1016/j.jweia.2018.01.029.

N. Nikitas and J. H. G. Macdonald. Aerodynamic forcing characteristics of dry cable galloping at critical Reynolds numbers. *European Journal of Mechanics, B/Fluids*, 49:243–249, 2015. doi: 10.1016/j.euromechflu.2014.09.005.

C. Norberg. Flow around rectangular cylinders: Pressure forces and wake frequencies. *Journal of Wind Engineering and Industrial Aerodynamics*, 49(1-3):187–196, 1993. doi: 10.1016/0167-6105(93)90014-F.

E. D. Obasaju. An investigation of the effects of incidence on the flow around a square section cylinder. *Aeronautical Quarterly*, 34, 1983.

A. Okajima. Strouhal numbers of rectangular cylinders. *Journal of Fluid Mechanics*, 123:379–398, 1982. doi: 10.1017/S0022112082003115.

V. Perrier, T. Philipovitch, and C. Basdevant. Wavelet spectra compared to Fourier spectra. *Journal of Mathematical Physics*, 36, 1995.

D. Prosser and M. J. Smith. Characterization of flow around rectangular bluff bodies at angle of attack. *Physics Letters A*, 376:3204–3207, 2012.

D. O. Rockwell. Organized fluctuations due to flow past a square cross section cylinder. *ASME Journal of Fluids Engineering*, 99, 1977.

A. Roshko. Perspectives on bluff body aerodynamics. *Journal of Wind Engineering and Industrial Aerodynamics*, 49:79–100, 1993.

A. Saha, K. Muralidhar, and G. Biswas. Experimental study of flow past a square cylinder at high Reynolds numbers. *Experiments in Fluids*, 29, 2000.

W. Sarwar and F. Mellibovskya. Characterization of three-dimensional vortical structures in the wake past a circular cylinder in the transitional regime. *Physics of Fluids*, 32, 2020. doi: 10.1063/5.0011311.

731 G. Schewe. Sensitivity of transition phenomena to small perturbations in flow round a circular
732 cylinder. *Journal of Fluid Mechanics*, 172:33–46, 1986. doi: 10.1017/S0022112086001635.

733 G. Schewe. Reynolds-number-effects in flow around a rectangular cylinder with aspect ratio 1:5.
734 *Journal of Fluids and Structures*, 39:15–26, 2013. doi: 10.1016/j.jfluidstructs.2013.02.013.

735 S. Szepessy and P. Bearman. Aspect ratio and end plate effects on vortex shedding from
736 a circular cylinder. *Journal of Fluid Mechanics*, 234:191–217, 1992. doi: 10.1017/
737 S0022112092000752.

738 B. J. Vickery. Fluctuating lift and drag on a long cylinder of square cross-section in a smooth
739 and in a turbulent stream. *Journal of Fluid Mechanics*, 25(3):481–494, 1966. doi: 10.1017/
740 S002211206600020X.

741 S. Wu, M. J.J., C. Hu, and J. Chou. On low-frequency modulations and three-dimensionality
742 in vortex shedding behind a normal plate. *Journal of Fluid Mechanics*, 526, 2005.

743 Q. Yang and Y. Tian. A model of probability density function of non-Gaussian wind pressure
744 with multiple samples. *Journal of Wind Engineering and Industrial Aerodynamics*, 140:
745 67–78, 2015.

746 Q. Yang, X. Chen, and M. Liu. Bias and sampling errors in estimation of extremes of non-
747 Gaussian wind pressures by moment-based translation process models. *Journal of Wind*
748 *Engineering and Industrial Aerodynamics*, 186:214–233, 2019.

749 T. Yang and M. S. Mason. Aerodynamic characteristics of rectangular cylinders in steady and
750 accelerating wind flow. *Journal of Fluids and Structures*, 90, 2019.